

A Dissection of the Topographic Effects from Eurasia and North America on the Isentropic Meridional Mass Circulation in Northern Winter

Yueyue Yu

Nanjing University of Information Science and Technology <https://orcid.org/0000-0001-9779-5732>

Rongcai Ren (✉ rrc@lasg.iap.ac.cn)

Institute of Atmospheric Physics Chinese Academy of Sciences

Xin Xia

Shenzhen Institute of Meteorological Innovation

Ruxue Liang

Nanjing University of Information Science and Technology

Jian Rao

Nanjing University of Information Science and Technology

Research Article

Keywords: Topographic, Eurasia, North America, Isentropic, Meridional Mass Circulation, Northern Winter, downstream wave pattern, meridional wind

Posted Date: September 29th, 2021

DOI: <https://doi.org/10.21203/rs.3.rs-826653/v1>

License:  This work is licensed under a Creative Commons Attribution 4.0 International License.

[Read Full License](#)

Version of Record: A version of this preprint was published at Climate Dynamics on January 14th, 2022.
See the published version at <https://doi.org/10.1007/s00382-021-06055-6>.

1 **A Dissection of the Topographic Effects from Eurasia and North America on the**
2 **Isentropic Meridional Mass Circulation in Northern Winter**

3

4 **Yueyue Yu^{1,2}, Rongcai Ren*^{2,1}, Xin Xia³, Ruxue Liang¹, Jian Rao^{1,4}**

5 ¹*Key Laboratory of Meteorological Disaster, Ministry of Education (KLME)/Joint*
6 *International Research Laboratory of Climate and Environment Change*
7 *(ILCEC)/Collaborative Innovation Center on Forecast and Evaluation of Meteorological*
8 *Disasters (CIC-FEMD) /NUIST-UoR International Research Institute, Nanjing University of*
9 *Information Science and Technology, Nanjing, China*

10 ²*State Key Laboratory of Numerical Modeling for Atmospheric Sciences and Geophysical*
11 *Fluid Dynamics (LASG), Institute of Atmospheric Physics, Chinese Academy of Sciences,*
12 *Beijing, China*

13 ³*Guangdong-Hong Kong-Macao Greater Bay Area Weather Research Center for Monitoring*
14 *Warning and Forecasting (Shenzhen Institute of Meteorological Innovation), Shenzhen,*
15 *China*

16 ⁴*Fredy and Nadine Herrmann Institute of Earth Sciences, Hebrew University of Jerusalem,*
17 *Israel*

18 Corresponding author: Rongcai Ren (rrc@lasg.iap.ac.cn), State Key Laboratory of Numerical
19 Modeling for Atmospheric Sciences and Geophysical Fluid Dynamics (LASG), Institute of
20 Atmospheric Physics, Chinese Academy of Sciences, Beijing, China

21

Abstract

The topographic dynamical effect from Eurasia (EA_Topo) and North America (NA_Topo) on the winter isentropic meridional mass circulation (IMMC) is investigated using the WACCM. The independent effect of EA_Topo and that of NA_Topo, with the former much stronger, are both to strengthen the IMMC that is composed of the lower equatorward cold air branch (CB) and the upper poleward warm air branch in the extratropical troposphere (WB_TR) and stratosphere (WB_ST). Further investigation of the individual contributions from changes in stationary vs. transient and zonal-mean flow vs. waves reveals that, due to the topography-forced mass redistribution, changes in the low-level meridional pressure gradient force a zonal-mean counter-clockwise/ clockwise meridional cell in the southern/northern side of topography. This weakens/strengthens the IMMC south/north of 30°N from the troposphere to lower stratosphere, acting as a dominant contributor to the IMMC changes south of 50°N. Meanwhile, the EA/NA_Topo-forced amplification of stationary waves constructively interacts with those determined by land-sea contrast, making the dominant/minor contributions to the strengthening of CB and WB_TR north of 50°N. The related increase in the upward wave propagation further dominates the WB_ST strengthening in the subpolar region. Meanwhile, transient eddy activities are depressed by EA/NA_Topo along with the weakened background westerly, which partly-offset/dominate-over the contribution from stationary flow in midlatitudes and subpolar region. The coexistence of the other topography (NA/EA_Topo) yields destructive mutual interference, which can weaken/offset the independent-EA/NA_Topo-forced meridional mass transport mainly via changing the zonal-mean as well as the downstream wave pattern of mass and meridional wind.

44 **1. Introduction**

45 The framework of Isentropic Meridional Mass Circulation (IMMC) was documented by
46 Johnson and his collaborators (Johnson 1989; Cai and Shin 2014 and references therein). The
47 IMMC represents a hemispheric cell which links the tropics to the poles and the troposphere
48 to the stratosphere via the poleward warm air branch (WB) in the upper troposphere (WB_TR)
49 and stratosphere (WB_ST) and the equatorward cold air branch in the lower troposphere
50 (CB). In the IMMC framework, a semi-Lagrangian and quantitative understanding has been
51 gained on the nature of the general atmospheric circulation (Chen 2013; Cai et al. 2014), on
52 the meridional heat and energy transport (Doos and Nilsson 2011; Pauluis et al. 2011;
53 Yamada and Pauluis 2015; Wu et al. 2019), and on the stratosphere–troposphere coupling
54 associated with oscillations of the polar vortex and jet (or the Northern Annular Modes) (Cai
55 and Ren 2006, 2007; Yu et al. 2014, 2015c, 2018a, b, c; Yu and Ren 2019). Moreover, the
56 intensity of CB across the polar circle is found to be closely related to winter cold air
57 outbreaks in the midlatitudes (Iwasaki and Mochizuki 2012; Iwasaki et al. 2014; Shoji et al.
58 2014). The WB always varies in phase with the CB and is recognized as a useful upper-level
59 precursor of cold air outbreaks (Yu et al. 2015a, b, c; Cai et al. 2016). Therefore,
60 investigating what dominates the intensity of IMMC and the underlying mechanisms can
61 provide insight on many widely known weather systems and climate patterns of interest.

62 The Northern Hemispheric IMMC is always stronger and wider in winter (Johnson 1989; Cai
63 and Shin 2014), when its driving force—the vertically westward tilted waves (Johnson
64 1989)—is stronger and more active. Among the wave forcings in the extratropics,
65 planetary-scale waves make the dominant contributions (Yu et al. 2018b). One of the major
66 sources of planetary waves is large-scale topography (Held et al. 2002; Smagorinsky 1953;
67 Nigam et al. 1986, 1988; Kasahara and Washington 1971; Manabe and Terpstra 1974; Lin
68 1982; Jacqmin and Lindzen 1985; Chen and Trenberth 1988; Sato et al. 2009). In Northern

69 Hemisphere (NH), the topography over Eurasia (EA_Topo hereafter), mainly composed of
70 the Tibetan Plateau, Iranian Plateau, and Mongolia Plateau, and the Rocky Mountains in the
71 west of North America (NA_Topo hereafter) play a critical role in intensifying stationary
72 planetary waves (Ringler and Cook 1995; Yanai et al. 2006) and enhancing their upward
73 propagation into the stratosphere (Zou et al. 1991a, b; Luo et al. 1985; Ding 1992; Taguchi
74 and Yoden 2002; Yanai et al. 2006; Gerber and Polvani 2009). The dynamical effect of
75 EA_Topo is much stronger than that of NA_Topo in determining the intensity and spatial
76 pattern of planetary waves (e.g., Held 1983; White et al. 2017). Park et al. (2013) pointed out
77 that the stationary waves forced by EA_Topo (e.g., the Tibetan Plateau) can constructively
78 interact with the preexisting stationary waves determined by land-sea contrast (Chang 2009),
79 thus making critical contributions to strengthen the poleward eddy heat transport over East
80 Asian and Eastern Pacific region. Accompanied with enhanced stationary waves by
81 topography, the transient eddy kinetic energy is reduced by topography (Manabe and Terpstra.
82 1974; Yu and Hartmann 1995; Son et al. 2009), and its compensation of the poleward energy
83 transport can be quite robust (Trenberth and Stepaniak 2003).

84 Most of the abovementioned studies focused on the topographic effects of EA_Topo or
85 NA_Topo with the other topography coexistent. The independent topographic effect and
86 possible mutual interference between them have not been well understood yet. A few linear
87 and nonlinear theoretical model studies (Luo et al. 1985; Held and Ting 1990; Valdes and
88 Hoskins 1991) suggested that either EA_Topo or NA_Topo may influence the topographic
89 forcing of the other on the atmospheric circulation by affecting the background zonal flow
90 across the NH. Ren et al. (2019) and Xia et al. (2019) recently carried out a series of
91 numerical experiments with the comprehensive Whole Atmosphere Community Climate
92 Model (WACCM) forced under different topographic conditions, and investigated the
93 independent (with the other topography nonexistent), the dependent (with the other

94 topography present), and the joint effects, as well as the mutual interference between
95 EA_Topo and NA_Topo in modulating the northern winter westerly jet and stratospheric
96 circulation. They found that the independent effects of EA_Topo and NA_Topo are both to
97 enhance the upward wave propagation and weaken the stratospheric polar vortex and polar jet.
98 Such independent effects tend to be destructively interfered due to the coexistence of the
99 other topography. Especially, the EA_Topo's interference can even offset the weakening
100 effect of NA_Topo on the stratospheric polar vortex (Ren et al. 2019). They provided a
101 primary explanation for the destructive mutual interference based on the stationary westerly
102 momentum responses in the troposphere in the upstream region of EA_Topo and NA_Topo,
103 and hence the weakened stationary wave responses due to the coexistence of the other
104 topography.

105 As a follow-up study of Ren et al. (2019), this study aims to first demonstrate the various
106 topographic effects on IMMC, whose stratospheric part is related to the stratospheric polar
107 vortex reported in Ren et al. (2019), and then to provide a physical understanding of the
108 topographic effects by performing a decomposition analysis on the IMMC responses to
109 topographic forcing. The isentropic analysis in the framework of IMMC can provide a clearer
110 picture of the dynamical role of topography in changing the atmospheric circulation. Firstly,
111 based on the surface potential temperature (mostly below 290K) in the spatial ranges of both
112 EA_Topo and NA_Topo (Fig. S1), the response of the CB (i.e., the equatorward branch
113 under 280~290K) can represent the direct topographic effect, as long as there are no
114 additional diabatic processes; Secondly, the topography-forced air mass redistribution
115 quantified by isentropic analysis makes it easier to understand the IMMC changes from
116 changes in meridional gradient of low-level pressure and temperature, and thus modulation
117 on the zonal-mean flow and planetary waves. Therefore, via numerical experiments,
118 isentropic analysis, and decomposition analysis, we try to answer two questions: i) What are

119 the changes in the three branches of IMMC in winter due to the various topographic forcing,
120 including the forcing of independent and dependent EA_Topo and NA_Topo, the joint
121 forcing, as well as the mutual interference between EA_Topo and NA_Topo? ii) How does
122 the topography modulate the stationary vs. transient and zonal-mean flow vs. waves and their
123 individual contributions to the total changes in IMMC?

124 This paper is organized as follows. Section 2 describes the data, model, and numerical
125 experiments, and the calculation scheme for the IMMC-related variables. In section 3, we
126 make deliberate parallel comparisons of the simulated fields of isentropic meridional mass
127 fluxes to demonstrate the independent effects of EA_Topo and NA_Topo and their mutual
128 interference on each branch of the IMMC in the NH. Then a decomposition analysis is
129 performed to diagnose the contributions to the IMMC responses to topographic forcing from
130 stationary vs. transient and zonal-mean flow vs. waves. Section 4 discusses the physical
131 processes related to stationary zonal-mean flow and waves, mainly via which the topography
132 takes effect. Conclusions and discussions about the topographic effect on the transient flow
133 are provided in section 5.

134 **2. Data and Methods**

135 ***2.1 Model and experiment design***

136 Version 4 of the WACCM (WACCM4) is used in this study. WACCM4 is a “high top”
137 model, with the model top reaching ~150 km (66 levels), and the horizontal resolution is 1.9°
138 $\times 2.5^\circ$ (latitude \times longitude) (Marsh et al. 2013). We conduct a seasonal run with
139 climatological monthly boundary condition (SST and sea ice), which is the key difference in
140 the numerical experiment design with that in Ren et al. (2019) and Xia et al. (2019), where
141 they use perpetual run. All experiments are integrated for 12,775 days, with a spin-up period
142 of 730 days discarded. Our following analysis will focus on the winter season, when the

143 dynamical effect of topography is the strongest, therefore, 32 winters (December-January-
144 February, DJF) of model data at 32 levels (1000, 925, 850, 700, 600, 500, 400, 300, 250, 200,
145 150, 100, 70, 50, 30, 20, 10, 7, 5, 3, 2, 1, 0.7, 0.5, 0.3, 0.2, 0.1, 0.07, 0.05, 0.03, 0.02, 0.01
146 hPa) are extracted and used.

147 As in Ren and Xia (2019) and Xia et al. (2019), we design four experiments: (i) the CTL run
148 (Fig. S2a), (ii) the experiment with the Rocky Mountains having been flattened (surface
149 higher than 500m in the region of 10–69°N, 90–160°W is flattened to 500m to keep the
150 smoothness of the basic platform as shown in Fig. S2b), denoted as noNA, (iii) similar
151 experiment with EA_Topo, including the Tibetan Plateau (26–40°N, 72–105°E), Iranian
152 Plateau (25–40°N, 40–75°E) and Mongolian Plateau (37–53°N, 87–122°E), having been
153 flattened (Fig. S2c), denoted as noEA, and (iv) the fourth experiment that flattens both
154 EA_Topo and NA_Topo, denoted as noEA&noNA (Fig. S2d). The “CTL minus
155 noEA&noNA” represents the joint effect of EA_Topo and NA_Topo. The “CTL minus
156 noNA” represents the topographic effect of NA_Topo with the coexistence of EA_Topo,
157 which indicates the “dependent” dynamical effect of NA_Topo on the circulation. Similarly,
158 the “CTL minus noEA” represents the “dependent” effect of EA_Topo. The “noNA minus
159 noEA&noNA” reveals the “independent” effect of EA_Topo when NA_Topo is nonexistent,
160 while the “noEA minus noEA&noNA” reveals the “independent” effect of NA_Topo. The
161 difference between the dependent and independent effects of NA/EA_Topo indicates the
162 effect of their mutual interference. To exclude the possible radiative effects of the strong
163 albedo due to the snow coverage over mountains in winter, we keep the same albedo,
164 roughness, and land cover in all of the four experiments. Therefore, by design, any
165 differences with the CTL run can be considered as the pure dynamical effects of EA_Topo
166 and NA_Topo.

167 **2.2 Calculation scheme of the IMMC-related variables**

168 The same methods as in Yu et al. (2015a, b) [also see Pauluis et al. (2008) and Cai and Shin
169 (2014)] are adopted to obtain the IMMC-related variables. The variable fields used for
170 calculation include daily surface air temperature (SAT), surface pressure (P_s), surface
171 meridional wind (v_s), and three-dimensional (3D) air temperature (T), meridional wind (v),
172 zonal wind (u), and geopotential height (z) fields. The 3D and surface potential temperature
173 (θ and θ_s) fields are derived from the daily fields of T, SAT, and P_s . The datasets used in this
174 study include not only the daily data obtained from the model experiments, but also those
175 derived from the six-hourly ERA-Interim data from January 1979 to December 2016
176 (ECMWF 2012; Simmons et al. 2007; Dee et al. 2011) on 1.5° latitude \times 1.5° longitude grids
177 and at 37 pressure levels from 1000 to 1 hPa.

178 *a. Isentropic layer mass*

179 Fifteen potential temperature surfaces Θ_n (n: 1–15) are preselected: 260, 270, 280, 290, 300,
180 315, 330, 350, 370, 400, 450, 550, 650, 850, and 1200 K. All variables are defined in the 14
181 layers between the Θ_n and Θ_{n+1} surfaces, plus two additional layers: one is the lowest layer,
182 which accounts for all air mass between the ground and 260 K, in case the surface potential
183 temperature at the grid is below 260 K; and the other is the top layer, which accounts for all
184 air mass above 1200 K. We use the bottom isentropic surface of each layer, i.e., Θ_n (n=1,14),
185 and 250 K and 1200 K respectively for the lowest and top layers in referencing the variables
186 defined in these isentropic layers.

187 The daily potential temperature and wind fields are interpolated onto 200 equally spaced
188 sigma (σ) levels from 1 to 0. The air mass between two adjacent sigma surfaces per unit area

189 is: $m_\sigma = \frac{\Delta\sigma}{g} P_s$, where g is the gravitational constant and $\Delta\sigma = 1/200$. We then derive the mass
 190 between two isentropic levels at each grid point on day t as

$$191 \quad M(\lambda, \phi, \Theta_n, t) = A(\phi) \cdot \int_0^1 m_\sigma(\lambda, \phi, \sigma, t) \cdot Y(\theta(\lambda, \phi, \sigma, t), \Theta_n, \Theta_{n+1}) d\sigma, \quad (1)$$

192 where λ is the longitude and ϕ is the latitude; $Y(x, x_1, x_2) = 1$ if $x_1 \leq x < x_2$, and otherwise
 193 $Y(x, x_1, x_2) = 0$; and $A(\phi)$ is the area of a grid box centered at the grid point. Via summing up
 194 the M along a given latitudinal band ϕ , we obtain the zonally integrated mass, and denote it
 195 using brackets, i.e., $[M]$. We further calculate the vertical sum of $[M]$ above each isentropic
 196 surface, which is proportional to the pressure at isentropic levels.

197 The winter mean $[M]$ pattern derived from the model CTL experiment largely resembles that
 198 in ERA-Interim (Fig. 1a), indicating the capability of WACCM4 in reproducing the
 199 characteristics of the meridional distribution of cold and warm air mass.

200 *b. Isentropic meridional mass fluxes*

201 We derive the meridional mass transport (MF) in the
 202 layer between two isentropic levels, Θ_n and Θ_{n+1} , at each grid point on day t in units of kg s^{-1}
 203 as

$$204 \quad MF(\lambda, \phi, \Theta_n, t) = A(\phi) \cdot \frac{\int_0^1 m_\sigma(\lambda, \phi, \sigma, t) \cdot v(\lambda, \phi, \sigma, t) \cdot Y(\theta(\lambda, \phi, \sigma, t), \Theta_n, \Theta_{n+1}) d\sigma}{R\Delta\phi}. \quad (2)$$

205 We further calculate and denote the zonally integrated MF as $[MF]$. Seen from the winter
 206 (DJF) climatology of $[MF]$ derived from ERA-Interim data (shadings in Fig. 1b), the winter
 207 mean $[MF]$ is positive/negative in the upper isentropic layers but negative/positive in the
 208 lower layers in the NH/Southern Hemisphere, indicating an isentropic meridional overturning
 209 mass circulation (IMMC) consisting of a poleward WB and an equatorward CB. The WB is

210 composed of the portion in the middle and upper troposphere (denoted as “WB_TR”) and that
 211 in the stratosphere (denoted as “WB_ST”). The winter mean [MF] pattern derived from the
 212 model CTL experiment (contours in Fig. 1b) largely resembles that derived from ERA-
 213 Interim Reanalysis data, except that the separating level between CB and WB where the
 214 strongest baroclinic instability exists in the model looks relatively colder than in the
 215 observation. Nevertheless, this systematic bias does not affect the results representing the
 216 dynamical roles of large-scale topography on the IMMC in this study.

217 *c. Separation of the warm and cold branches of IMMC*

218 The boundary level that separates the CB and WB of opposite directions at latitude ϕ and at
 219 day t is identified by searching for the isentropic level $\Theta_{n*}(\phi, t)$ such that the vertical sum of
 220 [MF] for all $n < n^*$ or $\Theta_n < \Theta_{n*}$ reaches its maximum negative value. As shown by the green
 221 curve in Fig. 1b, the isentropic surface of climatological mean $\Theta_{n*}(\phi, t)$ derived from CTL
 222 experiment effectively separates the CB and WB and decreases with increasing latitudes. The
 223 climatological mean $\Theta_{n*}(\phi, t)$ derived from the other three experiments are highly consistent.

224 Based on the tropopause temperature and pressure fields of NCEP/NCAR Reanalysis 1 in
 225 DJFs from 1979 to 2011, We derives the winter mean potential temperature near tropopause
 226 and then find the closest predefined isentropic level Θ_n (black curve in Fig. 1b) to indicate the
 227 approximate boundary level between WB_TR and WB_ST, denoted as $\Theta_{n**}(\phi, t)$.

228 With the two boundary isentropic levels obtained, the intensity of CB at each latitude can be
 229 measured by the vertical sum of [MF] below $\Theta_{n*}(\phi, t)$, the intensity of WB_TR can be
 230 measured by the vertical sum of [MF] from $\Theta_{n*}(\phi, t)$ to $\Theta_{n**-1}(\phi, t)$, and the intensity of
 231 WB_ST is measured by the vertical sum of [MF] from $\Theta_{n**}(\phi, t)$ to the top of the atmosphere.

232 *d. Spatial and temporal decomposition of the isentropic layer mass and its transport*

233 A Lorenz circulation resolution method (Lorenz 1967) is utilized, in which any variable at
 234 sigma levels, $X(\lambda, \phi, \sigma, t)$, can be decomposed into zonal-mean and wave components. The
 235 isentropic mass and meridional mass flux driven by zonal-mean flow can be derived as

$$236 \quad M_{\text{zonal}}(\phi, \Theta_n, t) = A(\phi) \cdot \int_0^1 \{m_\sigma\}(\phi, \sigma, t) \cdot Y(\{\theta\}(\phi, \sigma, t), \Theta_n, \Theta_{n+1}) d\sigma, \quad (3)$$

$$237 \quad MF_{\text{zonal}}(\phi, \Theta_n, t) = A(\phi) \cdot \frac{\int_0^1 \{m_\sigma\}(\phi, \sigma, t) \cdot \{v\}(\phi, \sigma, t) \cdot Y(\{\theta\}(\phi, \sigma, t), \Theta_n, \Theta_{n+1}) d\sigma}{R\Delta\phi}, \quad (4)$$

238 where the $\{ \}$ indicates the zonal-mean. The wave component of the isentropic mass and
 239 meridional mass flux can be obtained by removing the zonal-mean component from the total
 240 fields, namely,

$$241 \quad M_{\text{wave}}(\lambda, \phi, \Theta_n, t) = M(\lambda, \phi, \Theta_n, t) - M_{\text{zonal}}(\phi, \Theta_n, t), \quad (5)$$

$$242 \quad MF_{\text{wave}}(\lambda, \phi, \Theta_n, t) = MF(\lambda, \phi, \Theta_n, t) - MF_{\text{zonal}}(\phi, \Theta_n, t). \quad (6)$$

243 Before we further decompose the zonal-mean flow and wave components of MF into
 244 stationary and transient parts, we calculate the mass-weighted mean meridional wind velocity
 245 in a specific isentropic layer, denoted as V , which is proportional to the ratio of meridional
 246 mass flux to the mass in the same isentropic layer:

$$247 \quad V(\lambda, \phi, \Theta_n, t) = \frac{MF(\lambda, \phi, \Theta_n, t) \cdot R\Delta\phi}{M(\lambda, \phi, \Theta_n, t)}, \quad (7)$$

248 Similarly, the zonal-mean part of V (denoted as V_{zonal}) is equal to

$$249 \quad V_{\text{zonal}}(\phi, \Theta_n, t) = \frac{MF_{\text{zonal}}(\phi, \Theta_n, t) \cdot R\Delta\phi}{M_{\text{zonal}}(\phi, \Theta_n, t)}, \quad (8)$$

250 The wave part of V (denoted as V_{wave}) can be derived as the difference between the total and
 251 zonal-mean part of V :

$$252 \quad V_{\text{wave}}(\lambda, \phi, \theta_n, t) = V(\lambda, \phi, \theta_n, t) - V_{\text{zonal}}(\phi, \theta_n, t). \quad (9)$$

253 The MF driven by the total stationary flow (MF^s) and its zonal-mean part ($\text{MF}_{\text{zonal}}^s$) can be
254 respectively derived as

$$255 \quad MF^s(\lambda, \phi, \Theta_n) = \frac{\bar{V}(\lambda, \phi, \Theta_n, t) \cdot \bar{M}(\lambda, \phi, \Theta_n, t)}{R\Delta\phi}, \quad (10)$$

$$256 \quad MF_{zonal}^S(\phi, \Theta_n) = \frac{\bar{V}_{zonal}(\phi, \Theta_n, t) \cdot \bar{M}_{zonal}(\phi, \Theta_n, t)}{R\Delta\phi}, \quad (11)$$

where $(\cdot)^s$ indicates the stationary part, $(\overline{\cdot})$ denotes the 21-day running mean, and $(\overline{\overline{\cdot}})$ denotes the long-term climatological mean. The MF driven by stationary waves ($\text{MF}_{\text{wave}}^s(\lambda, \phi, \Theta_n)$) can be obtained by removing the $\text{MF}_{\text{zonal}}^s(\phi, \Theta_n)$ from $\text{MF}^s(\lambda, \phi, \Theta_n)$. Note that the 21-day running mean is chosen following Park et al. (2013) to include quasi-stationary waves such as Pacific-North America (PNA) pattern as stationary wave part, thus the transient eddies include mostly storm tracks.

263 The MF driven by transient flow ($MF^T(\phi, \Theta_n)$) is equal to either the residual of the MF after
 264 removing the MF^s or $\frac{V'(\lambda, \phi, \Theta_n, t) \cdot M'(\lambda, \phi, \Theta_n, t)}{R\Delta\phi}$, where ()' is the difference of daily fields from
 265 the 21-day running mean fields. Similarly, we can derive the MF due to the transient zonal-
 266 mean flow ($MF_{zonal}^T(\phi, \Theta_n)$) from the MF_{zonal} and MF_{zonal}^s . Finally, the MF driven by
 267 transient eddies ($MF_{wave}^T(\lambda, \phi, \Theta_n)$) can be obtained by removing the MF_{zonal}^T from MF^T .

268 3. Topography-forced changes in the NH IMMC

269 3.1 Zonally integrated meridional mass fluxes

270 We begin by comparing the features of IMMC among experiments. $\Delta()$ is used to denote the
 271 differences between them to present the change of a specific variable due to the topographic

272 forcing of EA_Topo and NA_Topo. Displayed in Fig. 2 are the latitudinal patterns of the
273 topography-forced $\Delta[\text{MF}]$ in various isentropic layers.

274 It can be seen from Fig. 2a that, the independent effect of EA_Topo is to significantly
275 strengthen the tropospheric portion of IMMC in the midlatitudes and subpolar region, as
276 manifested by the positive/negative $\Delta[\text{MF}]$ in the layers where the WB_TR/CB lies, but to
277 weaken it significantly in the low latitudes. Meanwhile, the independent effect of EA_Topo is
278 to strengthen the stratospheric portion of IMMC (WB_ST) across the entire NH, as seen from
279 the positive $\Delta[\text{MF}]$ covering the NH latitudes. The maximum strengthening of poleward [MF]
280 is around 45°N in the lower stratosphere but shifts poleward with increasing height. The
281 independent EA_Topo forced strengthening of IMMC can be seen more clearly from the
282 vertical integral of $\Delta[\text{MF}]$ in isentropic layers respectively within the CB, WB_TR, and
283 WB_ST (Figs. 3a, 4a, 5a).

284 The independent NA_Topo forced changes of CB and WB_TR show remarkable difference
285 with those forced by independent EA_Topo around 45–70°N, where the NA_Topo turns to
286 weaken the CB and WB_TR (Figs. 2c, 3c, and 4c). Though the hemispheric scale WB_ST is
287 still strengthened by the independent forcing of NA_Topo, the magnitudes of positive $\Delta[\text{MF}]$
288 are only ~1/4 of the those forced by the independent EA_Topo (Figs. 2c and 5c).

289 The topographic effect of mutual interference between EA_Topo and NA_Topo (Figs. 2f, 3f,
290 4f, and 5f) generally counteracts with their independent effects, characterized by a weakening
291 of both the WB_TR and CB in 20–50°N and the WB_ST in the extratropics. In the
292 troposphere, the magnitudes of $\Delta[\text{MF}]$ forced by mutual interference are comparable to those
293 forced by independent EA_Topo, and even larger than those forced by independent
294 NA_Topo. As a result, the EA_Topo-forced strengthening of CB and WB_TR becomes less
295 significant and limited within a narrower latitude band when the NA_Topo coexists (see

dependent effect of EA_Topo in Figs. 2b, 3b, and 4b), while the less remarkable strengthening effect of independent NA_Topo near 35–50°N is even offset to a significant weakening effect of CB and WB_TR in the entire extratropics when the EA_Topo coexists (Figs. 2d, 3d, and 4d). In the stratosphere, the magnitudes of $\Delta[\text{MF}]$ due to mutual interference are about 1/3 of those forced by independent EA_Topo but again much larger than those forced by independent NA_Topo. The independent-EA_Topo forced strengthening of WB_ST is thus slightly suppressed when the NA_Topo coexists (Fig. 5b), while that forced by independent NA_Topo is totally offset to a weakening of the WB_ST when the EA_Topo coexists (Fig. 5d).

In addition, because of the mutual interference in changing IMMC in both the troposphere and stratosphere, the $\Delta[\text{MF}]$ related to the joint effect of EA_Topo and NA_Topo (Figs. 2e, 3e, 4e, and 5e) is not a linear summation of their independent effects. The higher resemblance of the isentropic-latitudinal pattern of the joint effect to that of the EA_Topo's independent suggests the dominant role of EA_Topo in changing the IMMC.

Considering that the dependent as well as the joint effects of EA_Topo and NA_Topo can be inferred from their independent effects and mutual interference, and changes of WB_TR are highly coupled with changes of CB [as already demonstrated in Yu et al. (2015a) and confirmed by the overall out-of-phase changes of [MF] in the two branches shown in Figs. 2–4], our investigation in the following sections will mainly focus on the topographic effects of independent EA_Topo and independent NA_Topo and their mutual interference in changing the CB and WB_ST in NH.

3.2 Spatial-temporal decomposition of the IMMC responses to topography

To figure out individual contributions to the topography-forced IMMC changes, respectively from stationary and transient flow, both of which are composed of zonal-mean flow and

320 waves, we conduct a Lorenz spatial-temporal resolution analysis on the total $\Delta[\text{MF}]$ within
321 CB (Fig. 3) and WB_ST (Fig. 5).

322 We start with investigating the independent effects of EA_Topo and NA_Topo. It is seen
323 from Figs. 3a and 5a that the stationary component ($\Delta[\text{MF}^S]$) of the CB response to both the
324 independent forcing of EA_Topo and NA_Topo exhibits negative/positive values in the mid–
325 high/low latitudes. The $\Delta[\text{MF}^S]$ within WB_ST exhibits positive values across the entire NH
326 but large magnitudes in mid–high latitudes. The $\Delta[\text{MF}^S]$ forced by independent NA_Topo has
327 smaller magnitudes compared with that forced by independent EA_Topo. This indicates the
328 positive contributions of independent topography-forced stationary flow changes to the
329 significant strengthening of IMMC in the extratropical troposphere and stratosphere, with the
330 EA_Topo’s effect stronger than NA_Topo’s. A closer look at the stationary zonal-mean
331 ($\Delta[\text{MF}_{\text{zonal}}^S]$) and stationary wave ($\Delta[\text{MF}_{\text{wave}}^S]$) components yields that, in the region south of
332 50°N, the independent-EA_Topo-forced $\Delta[\text{MF}^S]$ in both the troposphere and stratosphere is
333 dominated by changes in zonal-mean flow; while north of 50°N, the strengthening of $\Delta[\text{MF}^S]$
334 is mainly contributed from changes in stationary waves. Seen from Figs. 3c and 5c, both the
335 topographic effect on both stationary zonal-mean and wave components are weaker
336 associated with the independent forcing of NA_Topo than that of EA_Topo, but the
337 weakening of the topographic effect is more severe for the wave component ($\Delta[\text{MF}_{\text{wave}}^S]$)
338 than the zonal-mean component ($\Delta[\text{MF}_{\text{zonal}}^S]$). As a result, the independent-NA_Topo-forced
339 $\Delta[\text{MF}^S]$ is dominated by $\Delta[\text{MF}_{\text{zonal}}^S]$ in the entire NH, whereas the $\Delta[\text{MF}_{\text{wave}}^S]$ makes minor
340 positive contributions in the region north of 45°N. The Independent-topography-forced
341 transient component of IMMC changes ($\Delta[\text{MF}^T]$), however, is always opposite to the
342 stationary component ($\Delta[\text{MF}^S]$). This supports the strong compensation between stationary
343 waves and transient eddies in their contributions to the meridional heat fluxes reported by

344 Trenberth and Stepaniak (2003). We further find that, the $\Delta[\text{MF}^T]$ is almost fully contributed
345 by its transient eddy component ($\Delta[\text{MF}_{\text{wave}}^T]$), while the magnitudes of its zonal-mean
346 component ($\Delta[\text{MF}_{\text{zonal}}^T]$) are much smaller. The relative importance of $\Delta[\text{MF}^S]$ and $\Delta[\text{MF}^T]$ in
347 determining the $\Delta[\text{MF}]$ depends on various factors including topography forcing, the IMMC
348 branches, and the latitudes. To be specific, the Independent-EA_Topo-forced $\Delta[\text{MF}^S]$ is
349 always strong enough to overwhelm the $\Delta[\text{MF}^T]$ in the extratropics, dominating the changes
350 of both CB and WB_ST (Figs. 3a and 5a). However, the independent-NA_Topo-forced
351 changes in transient eddy component plays a dominant role in changing the CB north of 50°N
352 (Fig. 3c).

353 The $\Delta[\text{MF}]$ forced by mutual interference is dominated by its stationary component ($\Delta[\text{MF}^S]$),
354 which is nearly out-of-phase with the independent-EA_Topo-forced $\Delta[\text{MF}^S]$ but with smaller
355 magnitudes (Figs. 3f and 5f). The weakening of CB in 20–50°N dominated by $\Delta[\text{MF}^S]$ is
356 mainly contributed by the $\Delta[\text{MF}_{\text{zonal}}^S]$ component, while the positive/negative $\Delta[\text{MF}_{\text{wave}}^S]$ in
357 20–40°N also contributes. As to the WB_ST, $\Delta[\text{MF}^S]$ is dominantly contributed by the
358 $\Delta[\text{MF}_{\text{zonal}}^S]$ south of 50°N, but by the $\Delta[\text{MF}_{\text{wave}}^S]$ in high latitudes. This also indicates the
359 growing/decreasing importance of the contributions from the mutual-interference-forced
360 changes in stationary waves/zonal-mean flow from the troposphere to stratosphere.
361 Meanwhile, the transient eddies related to mutual interference lead to positive $\Delta[\text{MF}_{\text{wave}}^T]$ in
362 the CB layer around 40°N and 65°N but negative $\Delta[\text{MF}_{\text{wave}}^T]$ in the WB_ST layer north of
363 50°N. This implies an enhancement of the destructive effect of mutual interference on the
364 IMMC changes by independent-topography-forced transient eddies in these latitude bands.

365 We summarize in Table 1 the main features of the independent-topography-forced IMMC
366 changes in CB and WB_ST, and that related to the mutual interference between EA_Topo

367 and NA_Topo, as well as the relative contributions from the stationary vs. transient, and from
368 the zonal-mean flow vs. wave components.

369 **4. On the stationary component of the topography-forced IMMC changes**

370 ***4.1 Troposphere***

371 *a. Stationary zonal-mean flow*

372 As abovementioned, one of the major approaches for the topography to affect the
373 tropospheric portion of IMMC is by modifying the stationary zonal-mean flow ($\Delta[MF_{\text{zonal}}^S]$).
374 We can see a high consistency in the $\Delta[MF_{\text{zonal}}^S]$ (Figs. 3–5) with the zonal-mean meridional
375 wind velocity and mass stream function at pressure levels (Fig. 6), namely the
376 strengthening/weakening of the poleward WB_TR and equatorward CB in the mid-high/low
377 latitudes corresponds to a topography-forced clockwise/counterclockwise zonal-mean
378 meridional cell in the troposphere below 150 hPa. Next we try to figure out how the
379 topography forces such a zonal-mean meridional cell.

380 Displayed in Figs. 7a and 7c are the independent-topography-forced changes in the zonal
381 integrated isentropic air mass and its vertical sum above, which is proportional to the
382 isentropic pressure. It is seen that due to the existence of the EA_Topo and NA_Topo, there
383 exists significant loss of air mass in the latitude ranges of topography but gain of air mass to
384 the northern and southern sides in the lower isentropic layers. Meanwhile, the positive air
385 mass changes in the stratosphere above 315K north of 40°N collaboratively enhance the total
386 mass gain in the northern side of topography (the mass changes in the stratosphere are mainly
387 resulted from WB_ST changes driven by stationary waves, which will be discussed in section
388 4.2). This causes a significant decrease of surface and low-level pressure in the latitude
389 ranges of topography, but a significant increase of pressure to the northern and southern sides.
390 The resultant low-level meridional pressure gradient favors southward/northward zonal-mean

391 meridional wind in the northern/southern side of mountain below 700 hPa (Figs. 6a and 6c).
392 The convergence effect (around 30°N for EA_Topo and 35°N for NA_Topo) is compensated
393 by the upward motion and an opposite pattern of zonal-mean meridional wind in the mid-to-
394 upper troposphere (200–300hPa). Thus, a counterclockwise/clockwise zonal-mean
395 meridional cell in the low/mid-to-high latitudes is formed due to the existence of independent
396 EA_Topo or NA_Topo, contributing to weaken/strengthen the CB and WB_TR in the
397 low/mid-to-high latitudes, as have been presented by $\Delta[\text{MF}_{\text{zonal}}^S]$ in Figs. 3a, 4a, 3c, and 4c.

398 The different effects of NA_Topo and EA_Topo, namely the much weaker and slightly
399 northward shifted low-level meridional gradient of pressure (cp. Figs. 7a and 7c) and thus the
400 forced zonal-mean meridional cell (cp. Figs. 6a and 6c), can be attributed to the smaller
401 volume as well as the northward location of NA_Topo than EA_Topo. It should be noted that,
402 the much less mass gain in the extratropical stratosphere forced by independent NA_Topo
403 also contributes to the weaker meridional gradient of low-level pressure.

404 As shown in Fig. 7f, the mutual interference acts to enhance/weaken the low-level air mass
405 export from the topography to its northern/southern side. This helps to increase/decrease the
406 surface pressure in the northern sides (45°–60°N)/southern sides (20°–45°N). However,
407 slightly above the surface, the column air mass or pressure changes are dominated by an
408 increase/decrease in the air mass above 315K in the region south/north of 40°N forced by
409 mutual interference, resulting in maximum positive/negative values of the vertical sum of [M]
410 or pressure at around 20°N/60°N. Therefore, the mutual interference leads to a
411 poleward/equatorward pressure gradient and thus the zonal-mean meridional wind in 20–
412 60°N/0–20°N at low levels (contours in Figs. 6f and 7f). Together with the opposite-signed
413 changes in the zonal-mean meridional wind in the upper layer, a counterclockwise meridional
414 cell in the midlatitudes (20–60°N) and a clockwise meridional cell in the low latitudes (0–

415 20°N) are formed due to the mutual interference, which is almost opposite to the meridional
416 cell forced by independent EA_Topo and NA_Topo. The magnitudes of the mutual-
417 interference-forced zonal-mean meridional cell are smaller than those of the EA_Topo-forced
418 meridional cell, but comparable with or even larger than the NA_Topo-forced meridional cell.
419 Therefore, the EA_Topo-forced clockwise meridional cell in the midlatitudes is slightly
420 weakened when the NA_Topo coexists (Fig. 6b); the NA-forced clockwise meridional cell in
421 the midlatitudes is offset and almost reversed while the counterclockwise meridional cell in
422 the subtropics is strengthened and extends northward (Fig. 6d). This explains the different
423 responses of the stationary zonal-mean component of CB and WB_TR to the topographic
424 forcing of EA_Topo and NA_Topo between without and with the other topography
425 coexistent (cp. Figs. 3b, 4b with 3a and 4a and cp. Figs. 3d and 4d with Figs. 3c and 4c).

426 *b. Stationary waves*

427 Stationary waves have crucial contributions to the strengthening of tropospheric branches of
428 IMMC in the midlatitudes and subpolar region. To understand how the existence of
429 topography and the mutual interference change the stationary waves as well as their resultant
430 meridional mass transport in the troposphere, we first focus on the CB layer, where the air
431 mass and its transport are directly affected by the uplifting, obstructing, and deflections of
432 both mountains.

433 The stationary wave pattern of the total air mass within the CB is equivalent to the long-term
434 average of the vertical integral of $M_{\text{wave}}(\lambda, \phi, \Theta_n, t)$ below the boundary level between cold
435 and warm branches of the IMMC ($\overline{\Theta_{n*}(\phi, t)}$). The stationary wave component of the mass-
436 weighted meridional wind in the CB ($V_{\text{CB}}^S_{\text{wave}}(\lambda, \phi)$) can be obtained based on eq. (7–9) by
437 substituting the isentropic layer mass and meridional mass fluxes with the vertical integral of
438 mass and meridional mass fluxes within the CB layer. The stationary part of mass-weighted

439 mean zonal wind velocity within the CB ($U_{CB^S}(\lambda, \phi)$) can be derived in the similar fashion
 440 to the $V_{CB_{wave}^S}$ by substituting the v with u . Then, the MF driven by independent-
 441 topography-forced stationary waves within the CB can be approximately linearized as,

$$442 \quad \Delta(\sum^{\overline{\Theta_{n*}(\phi,t)^{-1}}} \text{MF}_{\text{wave}}^S(\lambda, \phi, \Theta_n, t)) \approx \Delta M_{CB_{\text{wave}}^S} \cdot \Delta V_{CB_{\text{wave}}^S} + M_{CB_{\text{wave}}^S} \cdot \\ 443 \quad \Delta V_{CB_{\text{wave}}^S} + \Delta M_{CB_{\text{wave}}^S} \cdot V_{CB_{\text{wave}}^S}, \quad (12)$$

444 where the first term at the righthand side of eq. (12) denotes the spatial coherence between
 445 the $\Delta V_{CB_{\text{wave}}^S}$ (Figs. 8c and 8g) and $\Delta M_{CB_{\text{wave}}^S}$ (Figs. 9c and 9g) due to the independent
 446 topographic effect, the second term indicates the spatial coherence between the independent-
 447 topography-forced $\Delta V_{CB_{\text{wave}}^S}$ and the preexisting $M_{CB_{\text{wave}}^S}$ associated with land-sea
 448 contrast as shown in noEA&noNA experiment (Fig. 9a), and the third term indicates the
 449 spatial coherence between the preexisting $V_{CB_{\text{wave}}^S}$ (Fig. 8a) and the independent-
 450 topography-forced $\Delta M_{CB_{\text{wave}}^S}$.

451 Next let us briefly discuss the eq. (12) term by term, which are displayed in Figs. 10a–10c, to
 452 understand the independent effect of EA_Topo on the stationary wave component of the CB
 453 that is shown in Fig. 10d:

454 i) The first term ($\Delta M_{CB_{\text{wave}}^S} \cdot \Delta V_{CB_{\text{wave}}^S}$) tends to strengthen the equatorward CB in the
 455 extratropics except a narrow latitude band around 40°N. Seen from Fig. 8c, the mid-latitude
 456 westerly within the CB layer is weakened most severely in the upstream region of EA_Topo
 457 (90°W–90°E, 45°–70°N). Such weakening is accompanied by the strengthening of
 458 southerly/northerly in the latitudes north/south of 40°N on the windward side of EA_Topo
 459 and the strengthening of westerly to both the north and south of EA_Topo. This presents the
 460 mid-latitude westerly flow being blocked, deflected, and split into two branches due to the
 461 existence of EA_Topo. On the lee side, there is significantly strengthened northerly from the

462 polar region to the southeastern China and southerly from lower latitudes. The downstream
 463 effects can be seen from the alternating positive and negative values of $\Delta V_{CB_{wave}^S}$ farther
 464 downstream, covering the entire mid-latitude circles. As to the independent effect of
 465 EA_Topo on the air mass distribution, we see from Fig. 9c that around 30°N, where the peak
 466 of EA_Topo mainly locates, there is a significant reduction of $M_{CB_{wave}^S}$ in the mountain
 467 range but an increase in the other longitude bands. Besides, the EA_Topo-forced $\Delta M_{CB_{wave}^S}$
 468 tends to have an opposite sign to the $\Delta V_{CB_{wave}^S}$, with a slight westward shift relative to the
 469 $\Delta V_{CB_{wave}^S}$. This is because stronger northerlies always bring more cold air mass while
 470 stronger southerlies bring more/less warm/cold air mass in the midlatitudes, where the
 471 westerly flow is weakened due to the existence of EA_Topo. Therefore, the independent-
 472 EA_Topo-forced $\Delta M_{CB_{wave}^S} \cdot \Delta V_{CB_{wave}^S}$ tends to be mostly dominated by negative values
 473 over the extratropical Eurasia (Fig. 10a), implying a strengthening of the equatorward mass
 474 transport within the CB. However, in the region around 40°N and 90–120°E, the low-level air
 475 mass loss is severe because of the uplifting of the mountain and the $\Delta V_{CB_{wave}^S}$ is
 476 significantly equatorward there. The other region with significantly positive $\Delta M_{CB_{wave}^S} \cdot$
 477 $\Delta V_{CB_{wave}^S}$ is the western north Pacific region. The positive $\Delta M_{CB_{wave}^S} \cdot \Delta V_{CB_{wave}^S}$ in these
 478 two regions helps weaken the CB around 40°N.

479 ii) The second term ($M_{CB_{wave}^S} \cdot \Delta V_{CB_{wave}^S}$) is negative over the midlatitudes and subpolar
 480 region of East Asia and Europe respectively upstream and downstream of EA_Topo, playing
 481 a dominant role in strengthening the CB in the extratropics (Fig. 10b). This is because there is
 482 a significant out-of-phase patterns of the independent-EA_Topo-forced $\Delta V_{CB_{wave}^S}$ (Fig. 8c)
 483 and the preexisting $M_{CB_{wave}^S}$ that has larger magnitudes than $\Delta M_{CB_{wave}^S}$ (Fig. 9a) over the
 484 Eurasian continent.

485 iii) The third term ($\Delta M_{CB_{wave}^S} \cdot V_{CB_{wave}^S}$) also helps to strengthen the CB in the
 486 midlatitudes, indicated by an out-of-phase pattern of independent-EA_Topo-forced
 487 $\Delta M_{CB_{wave}^S}$ (Fig. 9c) and preexisting $V_{CB_{wave}^S}$ (Fig. 8a) over the east coast of Eurasia and
 488 some regions in the western hemisphere but with smaller magnitudes than $M_{CB_{wave}^S} \cdot$
 489 $\Delta V_{CB_{wave}^S}$. However, as the term $\Delta M_{CB_{wave}^S} \cdot \Delta V_{CB_{wave}^S}$, the preexisting equatorward wind
 490 brings severely decreased cold air mass over the mountain ranges (90–120°E, 30–50°N),
 491 which offsets the negative values of $\Delta M_{CB_{wave}^S} \cdot V_{CB_{wave}^S}$ over the rest longitudes around
 492 40°N.

493 Therefore, the $M_{CB_{wave}^S} \cdot \Delta V_{CB_{wave}^S}$, which represents the constructively interaction of the
 494 independent-EA_Topo-forced stationary wave pattern of meridional wind with the stationary
 495 wave pattern of cold air mass determined by land-sea thermal contrast, makes the largest
 496 contributions to strengthen the stationary wave component of CB in the extratropics, while
 497 the other two terms involving the independent-EA_Topo-forced cold air mass changes
 498 ($\Delta M_{CB_{wave}^S} \cdot \Delta V_{CB_{wave}^S}$ and $\Delta M_{CB_{wave}^S} \cdot V_{CB_{wave}^S}$) can explain the minimum
 499 strengthening of CB around 40°N.

500 Similar story can be told for the independent effect of NA_Topo (Figs. 8g, 9g, and 10e–10h).
 501 But the magnitudes of independent-NA_Topo-forced $\Delta V_{CB_{wave}^S}$ and $\Delta M_{CB_{wave}^S}$ are much
 502 smaller than those forced by EA_Topo. In addition, the independent-NA_Topo-forced
 503 $\Delta V_{CB_{wave}^S}$ is more local than the EA_Topo, manifested by the alternating positive and
 504 negative values of $\Delta V_{CB_{wave}^S}$ covering only 1/3 of the latitude band (furthest impact to
 505 60°E). Therefore, the strengthening of CB by independent-NA_Topo-forced stationary waves
 506 is less significant compared to the independent effect of EA_Topo (Fig. 3c).

507 Next let us look at the mutual interference between the EA_Topo and NA_Topo. Recall that
 508 the stationary wave changes due the mutual-interference are to weaken the CB in 20–50°N
 509 but slightly strengthen it in 50–65°N. Now the $\Delta V_{CB_{wave}^S}$ and $\Delta M_{CB_{wave}^S}$ in eq. (12)
 510 represent the changes forced by the dependent topography (Figs. 8f and 8h, 9f and 9h), while
 511 the preexisting fields, $M_{CB_{wave}^S}$ and $V_{CB_{wave}^S}$, are associated with land-sea contrast with
 512 the coexistence of the other topography (Figs. 8d and 9d for EA_Topo’s dependent effect and
 513 Figs. 8b and 9b for NA_Topo’s dependent effect). Each term in eq. (12) is displayed in Fig.
 514 11.

515 Firstly, we will address how the EA_Topo severely interferes with the dynamical effect of
 516 NA_Topo on the intensity of CB driven by stationary waves. As we all know, the EA_Topo
 517 is characterized by its highest altitudes over the world but relatively narrower meridional
 518 scale. With the existence of EA_Topo, the massive air in the lower isentropic layers replaced
 519 by the mountain has to spread out to other longitudes (Fig. 9c), leading to a significant
 520 increase of the preexisting $M_{CB_{wave}^S}$ around 30–45°N in the upstream region of NA_Topo
 521 (cp. Figs. 9b and 9a). Such increased amount of air mass approaching the windward side of
 522 NA_Topo favors a stronger deflection effect of NA_Topo, as indicated by a significantly
 523 strengthened southerly/northerly north/south of 45°N near the western boundary of NA_Topo
 524 that is accompanied with a strengthened northerly/southerly north/south of 30°N on the lee
 525 side of NA_Topo (cp. Figs. 8h and 8g). We see a farther extended stationary wave pattern of
 526 both $\Delta V_{CB_{wave}^S}$ and $\Delta M_{CB_{wave}^S}$ forced by NA_Topo when EA_Topo coexists, compared to
 527 that forced by independent NA_Topo. Such strengthened meridional wind exhibits an overall
 528 out-of-phase relationship with the preexisting $M_{CB_{wave}^S}$ in the downstream region of
 529 NA_Topo, thus it acts as a dominant contributor to the strengthening of CB in 40–65°N (Fig.
 530 11f). The mutual-interference-forced weakening of CB in 20–40°N, however, is mainly

531 contributed by the positive $V_{\text{CB}}^S \cdot \Delta M_{\text{CB}}^S$ over the midlatitude regions of East
 532 Pacific and North America. It is because the more air mass approaching the windward side of
 533 NA_Topo because of the coexistence of EA_Topo allows a much significant deduction of air
 534 mass over the spatial range of NA_Topo (cp. Fig. 9h with 9g or their difference shown in Fig.
 535 9i). Accompanied with this additional mass loss (negative ΔM_{CB}^S) are the strong
 536 preexisting northerlies (negative values of V_{CB}^S shown in Fig. 8b). This results in large
 537 positive values of $V_{\text{CB}}^S \cdot \Delta M_{\text{CB}}^S$, making dominant contributions to the weakening
 538 of the equatorward CB in 20–40°N (Fig. 11g).

539 The interference of NA_Topo with the dynamical effect of EA_Topo in changing the
 540 stationary waves in the CB layer, however, is quite weak. Compared to EA_Topo, NA_Topo
 541 has much lower altitudes and a much larger meridional scale. The air mass redistribution by
 542 NA_Topo covers almost all the NH latitudes, but with much smaller magnitudes compare to
 543 that by EA_Topo, particularly those around 30–45°N (cp. Fig. 9g and Fig. 9c).
 544 Correspondingly, the EA_Topo-forced changes in the wind fields also exhibit trivial
 545 difference between with and without the coexistence of NA_Topo (cp. Figs. 8c and 8f). In
 546 regard of this, we skip the detailed discussions on the NA_Topo’s interference with EA_Topo
 547 in modulating CB via changing stationary waves, though terms in eq. (12) presenting the
 548 EA_Topo’s dependent effect when NA_Topo coexists, are still displayed in Figs. 11a–d.

549 ***4.2 Stratosphere***

550 Unlike the tropospheric portion of IMMC that is directly modified by the topography via
 551 mechanical processes, the stratospheric portion is mainly modulated via the topography-
 552 forced quasi-stationary and planetary scale waves that can propagate upward. Following
 553 Zhang et al. (2013), we first calculated the daily amplitude of quasi-stationary waves at
 554 pressure levels as the root mean square of the zonal deviations of 21-day running mean fields

555 of geopotential height, and then obtained the long-term mean wave amplitude on isentropic
556 surfaces after linear interpolation based on the potential temperature at pressure levels.

557 It can be seen from Fig. 12a that the independent effect of EA_Topo is to increase the
558 amplitudes of stationary waves in the midlatitudes in lower isentropic layers. This can be
559 explained by the pattern coherence of the preexisting M_CB_{wave}^S (Fig. 9a) with the
560 independent-EA_Topo-forced ΔM_CB_{wave}^S (Fig. 9c) over the mid-latitude Eurasian continent
561 and Western Pacific region. Such amplified signals of large-scale stationary planetary waves
562 enhance upward wave propagation into the upper stratosphere following the poleward wave
563 guide (Huang and Gambo 1981, 1982; Chen et al. 2003, 2005). This is consistent with the
564 independent-EA_Topo-forced strengthened upward EP fluxes reported in Ren et al. (2019).
565 The stationary waves with larger amplitudes strengthen the poleward mass transport
566 ($\Delta[\text{MF}_{\text{wave}}^S]$), making dominant contributions to strengthen the WB_ST north of 50°N (Fig.
567 5a). Note that the independent-EA_Topo-forced maximum increase in the wave amplitude
568 shifts poleward with height, explaining the similar poleward shifting feature found in the
569 latitude bands with positive values of $\Delta[\text{MF}]$ at stratospheric levels (Fig. 2a). Such changes in
570 the meridional mass transport dominantly lead to positive/negative changes of stratospheric
571 air mass in the northern/southern side of the maximum strengthening of [MF] (Fig. 7a), which
572 plays an important role in determining the low-level pressure as mentioned in the previous
573 section 4.1a.

574 In the region south of 50°N, however, the topography-forced zonal-mean stationary
575 meridional wind plays a dominant role in changing the WB_ST (Fig. 5a). The latitude band
576 of 30–50°N with positive values of vertical integral of $\Delta[\text{MF}_{\text{zonal}}^S]$ in the WB_ST layer (Fig.
577 5a) is consistent with the topography-forced zonal-mean northward wind in the lower
578 stratosphere (Fig. 6a). We can tell that such northward zonal-mean wind is affected by the

579 topography-forced zonal-mean meridional cell in the troposphere, since the independent-
580 EA_Topo-forced zonal-mean northward wind in 30–50°N extends upward to the lower
581 stratosphere (up to 50 hPa). It is also noted that the zonal-mean flow in the upper stratosphere
582 (above 50hPa) is poleward in the midlatitudes but equatorward in the high latitudes (Fig. 6a).
583 This is because the maximum intensification of poleward mass transport by the EA_Topo-
584 forced stationary waves locates near the polar circle, which implies local
585 divergence/convergence to its southern/northern side. This requires poleward/equatorward
586 mass transport from higher/lower latitudes to compensate the local mass and accompanied
587 pressure changes. Nevertheless, such wave-driven changes in the zonal-mean meridional cell
588 in the upper stratosphere does not dominate the changes in the contributions from forced
589 zonal-mean flow to the entire WB_ST because of the rareness of air mass there.

590 The same story can be said for the topographic effects of NA_Topo on the WB_ST. The
591 independent-NA-forced $\Delta M_{CB_{wave}^S}$ pattern (Fig. 9c) is in phase with the preexisting
592 $M_{CB_{wave}^S}$ (Fig. 9a) over the midlatitude region of North America, which leads to larger wave
593 amplitudes in the lower isentropic layers and stronger upward propagation into the
594 stratosphere (Fig. 12c). The positive changes in wave amplitude forced by independent
595 NA_Topo are much smaller than that forced by independent EA_Topo, which corresponds to
596 much weaker positive changes in $\Delta[MF_{wave}^S]$ within the WB_ST in the midlatitudes (Fig. 5c)
597 as well as the related mass changes in the stratospheric layers (Fig. 7c). The less gain of
598 stratospheric mass in the higher latitudes due to independent NA_Topo also contributes to the
599 smaller equatorward pressure gradient at low levels thus consequently zonal-mean meridional
600 cell forced by NA_Topo than EA_Topo, as we have discussed above. Possibly because of the
601 weaker intensity of the NA_Topo-forced zonal-mean meridional cell, the altitude that the
602 NA_Topo-forced zonal-mean northward wind in midlatitudes can extend to is much lower
603 than the EA_Topo-forced one (cp. Figs. 6c and 6a). This explains why the NA_Topo-forced

strengthening of WB_ST dominated by zonal-mean flow in low and middle latitudes is also much weaker than the EA_Topo's effect (cp. $\Delta[\text{MF}_{\text{zonal}}^S]$ in Figs. 5c and 5a).

The mutual interference weakens the in-phase coherence of the preexisting M_CB_{wave}^S pattern with the topography-forced $\Delta\text{M}_{\text{CB}_{\text{wave}}^S}$ mainly in the mid-latitude regions of central Asia and the eastern North America (Fig. 9f), resulting in a less amplification of the stationary waves (Fig. 12f) as well as the related $\Delta[\text{MF}_{\text{wave}}^S]$ in the midlatitudes and subpolar region. The $\Delta[\text{MF}_{\text{wave}}^S]$ causes a $\Delta[\text{M}]$ pattern almost opposite to that forced by independent EA_Topo, which dominates the reversed meridional gradient of low-level pressure (Fig. 7f). As a result, the mutual-interference-forced zonal-mean meridional cell is almost the opposite to that forced by independent EA_Topo (Fig. 6f). And in addition, the equatorward zonal-mean meridional wind can also extend to the lower stratosphere, acting to weaken the stationary zonal-mean component of WB_ST. Therefore, the effect of mutual interference counteracts with the independent effect of EA_Topo and NA_Topo via modifying both the stationary zonal-mean flow in the midlatitudes as well as stationary waves in the subpolar region (Fig. 5f). The effect of mutual interference is weaker than the effect of independent EA_Topo on the stratospheric stationary flow, but strong enough to overwhelm the effect of independent NA_Topo, explaining the dependent effects of EA_Topo and NA_Topo in changing the stationary component of WB_ST when the other topography coexists (Figs. 5b and 5d).

5. Summary and discussions

5.1 Summary

This study investigates the dynamical effects of EA_Topo and NA_Topo in changing the Isentropic Meridional Mass Circulation in both the troposphere and stratosphere in NH winter, which is physically linked to global mass and energy transport, the polar vortex variability,

628 cold air outbreaks, etc. Via performing a series of numerical experiments with the
629 stratosphere-resolving WACCM, we examine not only the independent dynamical effects of
630 EA_Topo and NA_Topo but also their mutual interference, which further yields their
631 dependent effects when the other topography coexists stably and their joint effect. A Lorenz
632 circulation resolution method is then applied to diagnose the individual contributions from
633 changes in stationary vs. transient and zonal-mean flow vs. waves forced by various
634 topographic forcing to the IMMC changes. Finally, the physical processes related to
635 stationary flow mainly via which the topography takes effect are investigated.

636 A summary in Table 1 shows that the independent effects of both EA_Topo and NA_Topo
637 are to strengthen the equatorward cold and poleward warm branch of the IMMC in the
638 troposphere (CB and WB_TR) in the midlatitudes but to weaken them in the low latitudes.
639 The independent-NA-forced changes are much weaker than the independent-EA_Topo-
640 forced changes, in terms of both the magnitude and spatial span. Such changes of CB and
641 WB_TR south of 50°N are dominated by contributions from the topography-forced stationary
642 zonal-mean meridional cell, while those north of 50°N are dominated by contributions from
643 the topography-forced waves. The wave contributions are mainly from stationary waves for
644 the EA_Topo's effect but from transient eddies for the NA_Topo's effect. For the
645 stratospheric warm branch of IMMC (WB_ST) across the entire NH, the strengthening
646 effects of EA_Topo and NA_Topo are mainly contributed from the stationary zonal-mean
647 flow in the low and middle latitudes (south of 50°N/65°N) but from the stationary waves in
648 the high latitudes. When the other topography coexists, the mutual interference between
649 EA_Topo and NA_Topo is always destructive, which acts to weaken the independent-
650 EA_Topo-forced effect but completely offset the independent-NA_Topo-forced effect. It is
651 also found that such mutual interference takes effect mainly via changing stationary zonal-
652 mean flow south of 50°N and stationary waves north of 50°N.

653 We further investigated how the existence of EA_Topo and NA_Topo modifies the stationary
654 zonal-mean flow and stationary waves from the troposphere to stratosphere (as summarized
655 in Fig. 13). Firstly, the uplifting of either EA_Topo dominantly causes a decrease in the low-
656 level pressure over the spatial ranges of topography but an increase in the pressure both to the
657 north and to the south. This topography-forced meridional gradient of zonal-mean pressure
658 favors a clockwise/counterclockwise cell to the north/south of the topography, which yields a
659 strengthening/weakening of the CB and WB_TR in the middle/low latitudes. The
660 independent-EA_Topo-forced zonal-mean poleward flow in the upper troposphere can extend
661 to the lower stratosphere, dominantly contributing to the strengthening of the WB_ST in the
662 same latitude bands. Secondly, the blocking and deflecting effect of EA_Topo generates
663 strong stationary waves in the troposphere, via redistributing the surrounding air mass. The
664 topography-forced wave patterns of meridional flow and air mass changes constructively
665 interact with the preexisting wave patterns determined by land-sea contrast, contributing to
666 the strengthening of the equatorward CB and poleward WB_TR in the extratropics. The
667 topography-forced amplification of stationary planetary waves can propagate upward into the
668 stratosphere, leading to a strengthening of the poleward WB_ST in the subpolar region. And
669 the stratospheric mass exchange between lower and higher latitudes dominated by WB_ST
670 changes in the subpolar region can enhance the topographic effect on the meridional gradient
671 of low-level pressure and thus the zonal-mean meridional cell. All the abovementioned
672 processes in changing the IMMC can be said for NA_Topo, except that the NA_Topo-forced
673 changes are much weaker.

674 The destructive interference of one topography on the other is, on the one hand, mainly via
675 redistributing the air mass and changing the meridional flow in the downstream region of the
676 topography that is also the upstream region of the other topography, and consequently
677 weakening the large-scale stationary waves as well as their driven meridional mass fluxes in

the CB and WB_TR in the midlatitudes and subpolar region. On the other hand, the weakened large-scale stationary waves forced by the mutual interference can propagate upward to the stratosphere, weakening the WB_ST in the subpolar region. The weakened WB_ST in the subpolar region further decreases/increases the upper-level air mass in the mid–high/low latitudes, which dominates the meridional gradient of low-level pressure. Thus, the mutual interference forces a counterclockwise zonal-mean meridional cell in the midlatitudes from the troposphere to lower stratosphere, explaining the weakening of IMMC in the midlatitudes contributed by zonal-mean meridional flow due to mutual interference.

In the framework of isentropic meridional mass circulation, the results of this study help provide a comprehensive and clearer picture of the dynamical role of topography in changing the atmospheric circulation. A step further from Ren et al. (2009), we found that the topographic effects are achieved not only via modifying waves as many previous studies demonstrated (e.g., Yanai et al. 2006; Ding 1992; Park et al. 2013), but also via changing the zonal mean flow. The topographic effects on both the tropospheric circulation and the stratospheric circulation as well as their possible interaction, and the respective roles of stationary flow and transient eddies are also revealed. Investigation on the air mass and winds makes the underlying processes linking the surface topography and atmospheric circulation more physically direct to understand.

5.2 Discussions on the dynamical role of EA_Topo and NA_Topo in changing the transient eddy activities

It is still not answered yet, how the EA_Topo and NA_Topo change the transient eddies that also play an important role in changing the IMMC in the extratropics, particularly for the independent and dependent effects of NA_Topo. A previous study by Park et al. (2013) shows that the eady growth rate (EGR), which is widely used to estimate transient eddy

702 activity from the mean (Lindzen and Farrell 1980), is dominated by the EA_Topo-forced
703 zonal wind shear. Since the independent effects of both EA_Topo and NA_Topo are to slow
704 down the westerlies in the midlatitudes in both the troposphere and stratosphere (Ren et al.
705 2019), the EGR as well as the transient eddy activities are expected to be decreased by both
706 EA_Topo and NA_Topo. Our primary analysis has confirmed this conjecture for the
707 independent effects of EA_Topo and NA_Topo (see Figs. S3a and S3c), and the larger
708 magnitudes of the decrease in the independent-EA_Topo-forced EGR than that of the
709 independent-NA_Topo-forced EGR are also consistent with the more significant
710 independent-EA_Topo-forced weakening of the IMMC attributed to transient eddies (cp. Figs.
711 3a, 4a, 5a and Figs. 3c, 4c, 5c).

712 However, when considering the mutual interference, a clear inconsistency between the EGR
713 and IMMC changes related to transient eddies (cp. Fig. S3f with Figs. 3f, 4f, and 5f) can be
714 found in the subpolar stratosphere. Inconsistency between EGR and meridional heat flux is
715 also found by Park et al. (2013). The authors stated that this could be relevant to the nonlinear
716 interaction between stationary waves and transients including the upstream eddy seeding
717 effect on downstream transients (Penny et al. 2010; Son et al. 2009) and barotropic wind
718 shear on transients (Harnik and Chang 2004). Further investigation is needed to figure out
719 how the EA_Topo and NA_Topo changes the transient eddies and the resultant IMMC.

720 **Data Availability Statement**

721 The ERA-Interim datasets used in this work are available from the ECMWF ([http://www.](http://www.ecmwf.int)
722 [ecmwf.int](http://www.ecmwf.int)). The NCEP/NCAR Reanalysis 1 datasets are available from the NOAA
723 (<https://www.esrl.noaa.gov/psd/data/gridded/data.ncep.reanalysis.tropopause.html>).

724 **Acknowledgements**

725 This work was jointly supported by the Strategic Priority Research Program of the Chinese
726 Academy of Sciences (XDA17010105), National Natural Science Foundation of China
727 (42075052), and the National Key R&D Program of China (2019YFC1510201). We are
728 grateful for the availability of WACCM, provided by NCAR via the website
729 <http://www.cesm.ucar.edu/models/current.html>.

730 **References and citations:**

- 731 Cai M, Yu YY, Deng Y, Ven den Dool HM, Ren R, Saha S, Wu X, Huang J (2016) Feeling
732 the pulse of the stratosphere: An emerging opportunity for predicting continental-scale
733 cold-air outbreaks 1 month in advance. *Bull Amer Meteor Soc* 97:1475–1489
- 734 Cai M, Shin CS (2014) A total flow perspective of atmospheric mass and angular momentum
735 circulations: Boreal winter mean state. *J Atmos Sci* 71:2244–2263
- 736 Cai M, Ren RC (2006) 40–70 day meridional propagation of global circulation anomalies.
737 *Geophys Res Lett* 33: L06818. <http://doi.org/10.1029/2005GL025024>
- 738 Cai M, Ren RC (2007) Meridional and downward propagation of atmospheric circulation
739 anomalies. part I: Northern Hemisphere cold season variability. *J Atmos Sci* 64:1880–
740 1901
- 741 Chang EKM (2009) Diabatic and orographic forcing of northern winter stationary waves and
742 storm tracks. *J Climate* 22:670–688. <https://doi.org/10.1175/2008JCLI2403.1>
- 743 Chen G (2013) The Mean Meridional Circulation of the Atmosphere Using the Mass above
744 Isentropes as the Vertical Coordinate. *J Atmos Sci* 70:2197–2213
- 745 Chen SC, Trenberth KE (1988) Forced planetary waves in the Northern Hemisphere winter:
746 Wave-coupled orographic and thermal forcings. *J Atmos Sci* 45:682–704.
747 [https://doi.org/10.1175/1520-0469\(1988\)045<0682:FPWITN>2.0.CO;2](https://doi.org/10.1175/1520-0469(1988)045<0682:FPWITN>2.0.CO;2)
- 748 Chen W, Takahashi M, Graf H (2003) Interannual variations of stationary planetary wave
749 activity in the northern winter troposphere and stratosphere and their relations to NAM
750 and SST. *J Geophys Res* 108:D24
- 751 Chen W, Yang S, Huang RH (2005) Relationship between stationary planetary wave activity
752 and the East Asian winter monsoon. *J Geophys Res* 110:D14110
- 753 Dee DP, Uppala SM, Simmons AJ, Berrisford P, Poli P, Kobayashi S, Andrae U, Balsamo G,
754 Bauer P, Bechtold P, Beljaars ACM, Berg LVD, Bidlot J, Bormann N, Delsol C,

- 755 Dragani R, Fuentes M, Geer AJ, Haimberger L, Healy SB, Hersbach H, Holm EV,
756 Isaksen L, Kallberg P, Kohler M, Matricardi M, McNally AP, Monge-Sanz BM,
757 Morcrette JJ, Park BK, Peubey C, Rosnay PD, Tavolato C, Thepaut JN, Vitart F (2011)
758 The ERA-Interim reanalysis: Configuration and performance of the data assimilation
759 system. *Quart J Roy Meteor Soc* 137:553–597. <https://doi.org/10.1175/10.1002/qj.828>
- 760 Ding Y (1992) Effects of the Qinghai–Xizang (Tibetan) plateau on the circulation features
761 over the plateau and its surrounding areas. *Adv Atmos Sci* 9:112–130.
762 <https://doi.org/10.1007/BF02656935>
- 763 Doos K, Nilsson J (2011) Analysis of the Meridional Energy Transport by Atmospheric
764 Overturning Circulations. *J Atmos Sci* 68:1806–1820
- 765 ECMWF (2012) ERA Interim, daily. European centre for Medium-Range Weather Forecasts.
766 Subset used: 1 November 1979–28 February 2011.
767 <http://apps.ecmwf.int/datasets/data/interim-full-daily/>. Accessed 1 July 2012.
- 768 Gerber EP, Polvani LM (2009) Stratosphere–troposphere coupling in a relatively simple
769 AGCM: The importance of stratospheric variability. *J Climate* 22:1920–1933.
770 <https://doi.org/10.1175/2008JCLI2548.1>
- 771 Harnik N, Chang EKM (2004) The effects of variations in jet width on the growth of
772 baroclinic waves: Implications for midwinter Pacific storm track variability. *J Atmos Sci*
773 61:23–40
- 774 Held IM (1983) Stationary and quasi-stationary eddies in the extratropical troposphere:
775 Theory, Large-scale dynamical processes in the atmosphere 127–168.
776 <http://citeseerx.ist.psu.edu/viewdoc/download?doi=10.1.1.226.5733&rep=rep1&type=pdf>

- 778 Held IM, Ting M (1990) Orographic versus thermal forcing of stationary waves: The
779 importance of the mean low-level wind. *J Atmos Sci* 47:495–500.
780 [https://doi.org/10.1175/1520-0469\(1990\)047,0495:OVTFOS.2.0.CO;2](https://doi.org/10.1175/1520-0469(1990)047,0495:OVTFOS.2.0.CO;2)
- 781 Held IM, Ting M, Wang H (2002) Northern winter stationary waves: Theory and modeling. *J*
782 *Climate* 15:2125–2144. [https://doi.org/10.1175/1520-0442\(2002\)015<2125:NWSWTA>2.0.CO;2](https://doi.org/10.1175/1520-0442(2002)015<2125:NWSWTA>2.0.CO;2)
- 784 Huang RH, Gambo K (1981) The response of a model atmosphere in middle latitude to
785 forcing by topography and stationary heat sources. *J Meteor Soc Japan* 59:220–237
- 786 Huang RH, Gambo K (1982) The response of a hemispheric multi-level model atmosphere to
787 forcing by topography and stationary heat source. Part. I. *J Meteor Soc Japan* 60:88–92
- 788 Iwasaki T, Mochizuki Y (2012) Mass-weighted isentropic zonal-mean equatorward flow in
789 the Northern Hemispheric winter. *SOLA* 8:115–118. <https://doi.org/10.2151/sola.2012-029>
- 791 Iwasaki T, Shoji T, Kanno Y, Sawada M, Takaya K, Ujiie M (2014) Isentropic analysis of
792 polar cold air mass streams in the Northern Hemispheric winter. *J Atmos Sci* 71:2230–
793 2243. <https://doi.org/10.1175/JAS-D-13-058.1>
- 794 Jacqmin D, Lindzen R (1985) The causation and sensitivity of the northern winter planetary
795 waves. *J Atmos Sci* 42:724–746. [https://doi.org/10.1175/1520-0469\(1985\)042<0724:TCASOT>2.0.CO;2](https://doi.org/10.1175/1520-0469(1985)042<0724:TCASOT>2.0.CO;2)
- 797 Johnson DR (1989) The forcing and maintenance of global monsoonal circulations: An
798 isentropic analysis. *Adv in Geophys* 31:43–316
- 799 Kasahara A, Washington WM (1971) General circulation experiments with a six-layer NCAR
800 model, including orography, cloudiness and surface temperature calculations. *J Atmos*
801 *Sci* 28:657–701. [https://doi.org/5/1520-0469\(1971\)028<0657:GCEWAS>2.0.CO;2](https://doi.org/5/1520-0469(1971)028<0657:GCEWAS>2.0.CO;2)

- 802 Lin BD (1982) The behavior of winter stationary planetary waves forced by topography and
803 diabatic heating. *J Atmos Sci* 39:1206–1226. [https://doi.org/10.1175/1520-0469\(1982\)039<1206:TBOWSP>2.0.CO;2](https://doi.org/10.1175/1520-0469(1982)039<1206:TBOWSP>2.0.CO;2)
- 804
- 805 Lindzen R, Farrell B (1980) A simple approximate result for the maximum growth rate of
806 baroclinic instabilities. *J Atmos Sci* 37:1648–1654
- 807 Lorenz EN (1967) The nature and theory of the general circulation of the atmosphere. Vol
808 218, World Meteorological Organization Geneva
- 809 Luo M, Zhu B, Zhang X (1985) The dynamic effect of the Tibetan Plateau on the formation
810 of zonal type circulation over East Asia. *Adv Atmos Sci* 2:158–166.
811 <https://doi.org/10.1007/BF03179748>
- 812 Manabe S, Terpstra TB (1974) The effects of mountains on the general circulation of the
813 atmosphere as identified by numerical experiments. *J Atmos Sci* 31:3–42.
814 [https://doi.org/10.1175/1520-0469\(1974\)031<0003:TEOMOT>2.0.CO;2](https://doi.org/10.1175/1520-0469(1974)031<0003:TEOMOT>2.0.CO;2)
- 815 Marsh D. R, Janches D, Feng WH, Plane JMC (2013) A global model of meteoric sodium. *J*
816 *Geophys Res Atmos* 118:11442–11452
- 817 Nigam S, Held IM, Lyons SW (1986) Linear simulation of the stationary eddies in a general
818 circulation model. Part I: The no-mountain model. *J Atmos Sci* 43:2944–2961.
819 [https://doi.org/10.1175/1520-0469\(1986\)043<2944:LSOTSE>2.0.CO;2](https://doi.org/10.1175/1520-0469(1986)043<2944:LSOTSE>2.0.CO;2)
- 820 Nigam S, Held IM, Lyons SW (1988) Linear simulation of the stationary eddies in a GCM.
821 Part II: The “mountain” model. *J Atmos Sci* 45:1433–1452.
822 [https://doi.org/10.1175/1520-0469\(1988\)045<1433:LSOTSE>2.0.CO;2](https://doi.org/10.1175/1520-0469(1988)045<1433:LSOTSE>2.0.CO;2)
- 823 Park HS, Xie SP, Son SW (2013) Poleward Stationary Eddy Heat Transport by the Tibetan
824 Plateau and Equatorward Shift of Westerlies during Northern Winter. *J Atmos Sci*
825 70:3288–3301

- 826 Pauluis O, Czaja A, Korty R (2008) The global atmospheric circulation on moist isentropes.
827 Science 321:1075–1078. <https://doi.org/10.1126/science.1159649>
- 828 Pauluis O, Shaw T, Laliberté F (2011) A Statistical Generalization of the Transformed
829 Eulerian-Mean Circulation for an Arbitrary Vertical Coordinate System. J Atmos Sci
830 68:1766–1783
- 831 Penny SM, Roe G, Battisti D (2010) The source of the midwinter suppression in storminess
832 over the North Pacific. J Climate 23:634–648
- 833 Ren RC, Xia X, Rao J (2019) Topographic forcing from East Asia and North America in the
834 northern winter stratosphere and their mutual interference. J Climate 32:8639–8658.
835 <https://doi.org/10.1175/JCLI-D-19-0107.1>
- 836 Ringler T, Cook K (1995) Orographically induced stationary waves: Dependence on latitude.
837 J Atmos Sci 52:2548–2560. [https://doi.org/10.1175/1520-0469\(1995\)052<2548:OISWDO>2.0.CO;2](https://doi.org/10.1175/1520-0469(1995)052<2548:OISWDO>2.0.CO;2)
- 839 Sato K, Watanabe S, Kawatani Y, Tomikawa Y, Miyazaki K, Takahashi M (2009) On the
840 origins of mesospheric gravity waves. Geophys Res Lett 36:L19801
- 841 Shoji T, Kanno Y, Iwasaki T, Takaya K (2014) An isentropic analysis of the temporal
842 evolution of East Asian cold air outbreaks. J Climate 27:9337–9348.
843 <https://doi.org/10.1175/JCLI-D-14-00307.1>
- 844 Simmons A, Uppala S, Dee D, Kobayashi S (2007) ERA- Interim: New ECMWF reanalysis
845 products from 1989 onwards. ECMWF Newsletter No. 110, ECMWF, Reading, pp 25–
846 35
- 847 Smagorinsky J (1953) The dynamical influence of large - scale heat sources and sinks on the
848 quasi - stationary mean motions of the atmosphere. Quart J Roy Meteor Soc 79:342–
849 366. <https://doi.org/10.1002/qj.49707934103>

- 850 Taguchi M, Yoden S (2002) Internal interannual variability of the troposphere–stratosphere
851 coupled system in a simple global circulation model. Part I: Parameter sweep
852 experiment. *J Atmos Sci* 59:3021–3036. [https://doi.org/10.1175/1520-0469\(2002\)059<3021:IIVOTT>2.0.CO;2](https://doi.org/10.1175/1520-0469(2002)059<3021:IIVOTT>2.0.CO;2)
- 854 Trenberth KE, Stepaniak DP (2003) Covariability of components of poleward atmospheric
855 energy transports on seasonal and interannual timescales. *J Climate* 15:3691–3705
- 856 Valdes PJ, Hoskins BJ (1991) Nonlinear orographically forced planetary waves. *J Atmos Sci*
857 48:2089–2106
- 858 White R, Battisti D, Roe G (2017) Mongolian mountains matter most: Impacts of the latitude
859 and height of asian orography on pacific wintertime atmospheric circulation. *J Climate*
860 30:4065–4082. <https://doi.org/10.1175/JCLI-D-16-0401.1>
- 861 Wu Y, Lu J, Pauluis O (2019) Weakening of upward mass but intensification of upward
862 energy transport in a warming climate. *Geophys Res Lett* 46:1672–1680.
863 <https://doi.org/10.1029/2018GL081399>
- 864 Xia X, Ren RC, Yu YY (2019) Dynamical role of the Rocky Mountain controlled by East
865 Asian topographies in modulating the tropospheric westerly jet in northern
866 winter. *Atmos Oceanic Sci Lett* 12:66–72.
867 <https://doi.org/10.1080/16742834.2018.1548247>
- 868 Yamada R, Pauluis O (2015) Annular Mode Variability of the Atmospheric Meridional
869 Energy Transport and Circulation. *J Atmos Sci* 72:2070–2089
- 870 Yanai M, Wu GX, Wang B (2006) Effects of the tibetan plateau, in The Asian Monsoon,
871 edited, pp 513–549. https://doi.org/10.1007/3-540-37722-0_13
- 872 Yu YY, Cai M, Ren RC, Ven den Dool HM (2015a) Relationship between warm air mass
873 transport into upper polar atmosphere and cold air outbreaks in winter. *J Atmos Sci*
874 72:349–368

- 875 Yu JY, Hartmann DL (1995) Orographic influences on the distribution and generation of
876 atmospheric variability in a GCM. *J Atmos Sci* 52:2428–2443
- 877 Yu YY, Ren RC, Cai M (2015b) Dynamical linkage between cold air outbreaks and intensity
878 variations of the meridional mass circulation. *J Atmos Sci* 72:3214–3232
- 879 Yu YY, Ren RC, Cai M (2015c) Comparison of the mass circulation and AO indices as
880 indicators of cold air outbreaks in northern winter. *Geophys Res Lett* 42:2442–2448.
881 <https://doi.org/10.1002/2015GL063676>
- 882 Yu YY, Ren RC, Hu JG, Wu GX (2014) A mass budget analysis on the interannual variability
883 of the polar surface pressure in the winter season. *J Atmos Sci* 71:3539–3553.
884 <https://doi.org/10.1175/JAS-D-13-0365.1>
- 885 Yu YY, Cai M, Ren RC (2018a) A stochastic model with a low-frequency amplification
886 feedback for the stratospheric northern annular mode. *Climate Dynam* 9–10:3757–3773.
887 <https://doi.org/10.1007/s00382-017-3843-2>
- 888 Yu YY, Cai M, Shi CH, Ren RC (2018b) On the linkage among strong stratospheric mass
889 circulation, stratospheric sudden warming, and cold weather events. *Mon Wea Rev*
890 146:2717–2739
- 891 Yu YY, Cai M, Ren RC, Rao J (2018c) A closer look at the relationships between meridional
892 mass circulation pulses in the stratosphere and cold air outbreak patterns in northern
893 hemispheric winter. *Climate Dynam* 51:3125–3143
- 894 Zhang Q, Shin CS, Dool HMVD, Cai M (2013) CFSv2 prediction skill of stratospheric
895 temperature anomalies. *Clim Dynam* 41:2231–2249
- 896 Zou XL, Ye D, Wu GX (1991a) The Analysis Of Dynamic Effects On Winter Circulation Of
897 The Two Main Mountains In The Northern Hemisphere I. Circulation, Teleconnection
898 and Horizontal Propagation of Stationary Waves. *Acta Meteorol Sin* 49:129–140.
899 <https://doi.org/10.11676/qxb1991.021> (in Chinese)

900 Zou XL, Wu GX, Ye D (1991b) The Analysis Of Dynamic Effects On Winter Circulation Of
901 The Two Main Mountains In The Northern Hemisphere II. Vertical Propagation of
902 Planetary Waves. *Acta Meteorol Sin* 49:257–268. <https://doi.org/10.1007/BF02919618>
903 (in Chinese)

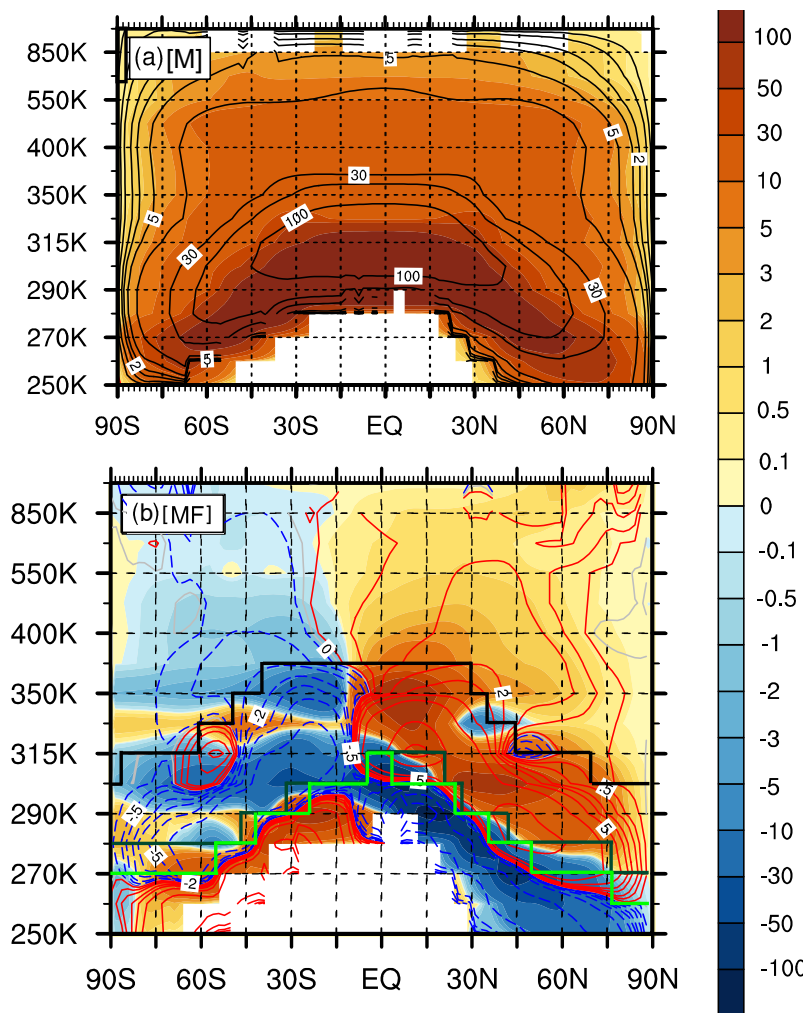
904 **Table 1.** Summary of the main changes in CB and WB_ST of IMMC forced by independent
 905 EA and NA topography and their mutual interference. The asterisks in the fourth column
 906 indicates that the changes in the specific component makes dominant contributions to the
 907 IMMC changes.

Topographic forcing	Topography-forced changes in IMMC		Topography-forced changes in decomposed components and their contributions to IMMC changes	
	Branch	Main facts	Component	Main facts
Independent EA	CB	Weakening south of 30°N;	Stationary zonal-mean flow*	Weakening south of 30°N and strengthening in 30–70°N; <i>Dominates the changes south of 50°N.</i>
		Strengthening in 30–70°N.	Stationary wave*	Strengtheneing in 15–80°N; <i>Dominates the changes north of 50°N.</i>
			Transient eddy	Weakening in 15–80°N.
	WB_ST	Strengthening in the NH (mainly in the mid and high latitudes)	Stationary zonal-mean flow*	Strengthening south of 65°N (mainly in the midlatitudes); <i>Dominates the changes south of 50°N.</i>
			Stationary wave*	Strengthening north of 45°N; <i>Dominates the changes north of 50°N.</i>
			Transient eddy	Weakening north of 35°N.
Independent NA	CB	Weakening in 10–35°N;	Stationary zonal-mean flow*	Weakening/strengthening in 10–35°N/35–70°N; <i>Dominates changes in the region south of 50°N</i>
		Slight strengthening in 35–50°N;	Stationary wave	Slight strengthenning in 15–70°N.
		Weakening in 50–70°N.	Transient eddy*	Weakening in 15–70°N; <i>Dominates the changes north of 50N.</i>
	WB_ST	Strengthening in NH (mainly in the mid and high latitudes)	Stationary zonal-mean flow*	Strengthening south of 70°N; <i>Dominates the region south of 65°N.</i>
			Stationary wave*	Slight strengthening north of 50°N; <i>Dominates the changes north of 65°N.</i>
			Transient eddy	Weakening in 40–75°N.
Mutual interference	CB	Strengthening/weakening in 5–20°N/20–50°N;	Stationary zonal-mean flow*	Strengthening/weakening in 5–20°N/20–50°N; <i>Dominates the region south of 50°N.</i>
		Slight strengthening/weakening in 50–65°N/65–75°N.	Stationary wave*	Weakening/strengthening in 20–40°N/50–65°N; <i>Dominates the region 50–65°N and make important contributions in 20–40°N.</i>
			Transient eddy*	Slight weakening around 35–50°N and 50–75°N; <i>Dominates the region north of 65–75 °N.</i>
	WB_ST	Weakening North of 30°N	Stationary zonal-mean flow*	Weakening/strengthening in 30–60°N/north of 60°N; <i>Dominates the region south of 50°N.</i>
			Stationary wave*	Weakening north of 50°N but slight strengthening in 30–50°N; <i>Dominates the changes north of 50°N.</i>
			Transient eddy	Slight weakening/strengthening in north

908

				of 50°N/30–50°N; <i>Also positively contributes to the changes north of 50°N.</i>
--	--	--	--	--

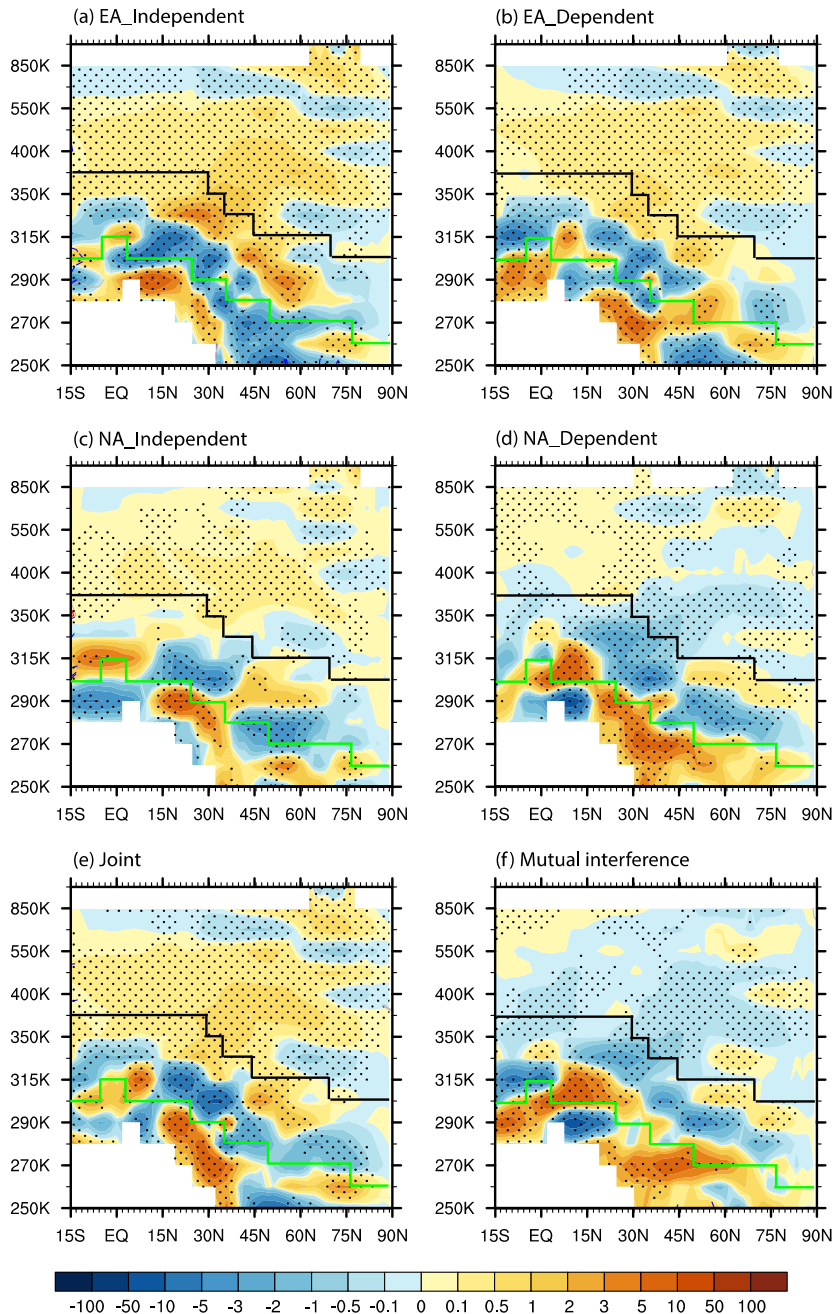
909

Figures:

910

911
912
913
914
915
916
917
918

Figure 1. Winter climatology of the zonally integrated (a) mass (units: 10^{14} kg) and (b) meridional mass flux (units: 10^9 kg s^{-1}) derived from ERA-Interim (shadings) and the CTL experiment of WACCM (contours). Black curve in panel (b) indicates the boundary isentropic level between troposphere and stratosphere based on the winter mean tropopause potential temperature derived from NCEP/NCAR Reanalysis-1, while the green/dark green curve indicates the winter mean boundary isentropic level between the equatorward CB and the poleward WB of the IMMC derived from the CTL experiment of WACCM/ERA-Interim.



919

Figure 2. Latitude-vertical patterns of the difference among the four experiments in the winter climatology (units: 10^9 kg s^{-1}) of the zonally integrated meridional mass flux ([MF]) to represent the dynamical effect of (a) independent EA, (b) dependent EA, (c) independent NA, (d) dependent NA, (e) the joint effect of EA and NA, and (f) their mutual interference [(b) minus (a) or (d) minus (c)]. Dotted areas mark the 95% confidence level from a Student's *t*-test. Black and green curves respectively indicate the approximate climatological mean boundary isentropic level between the WB_TR and WB_ST and the boundary isentropic level between the CB and WB_TR as shown in Fig. 2b.

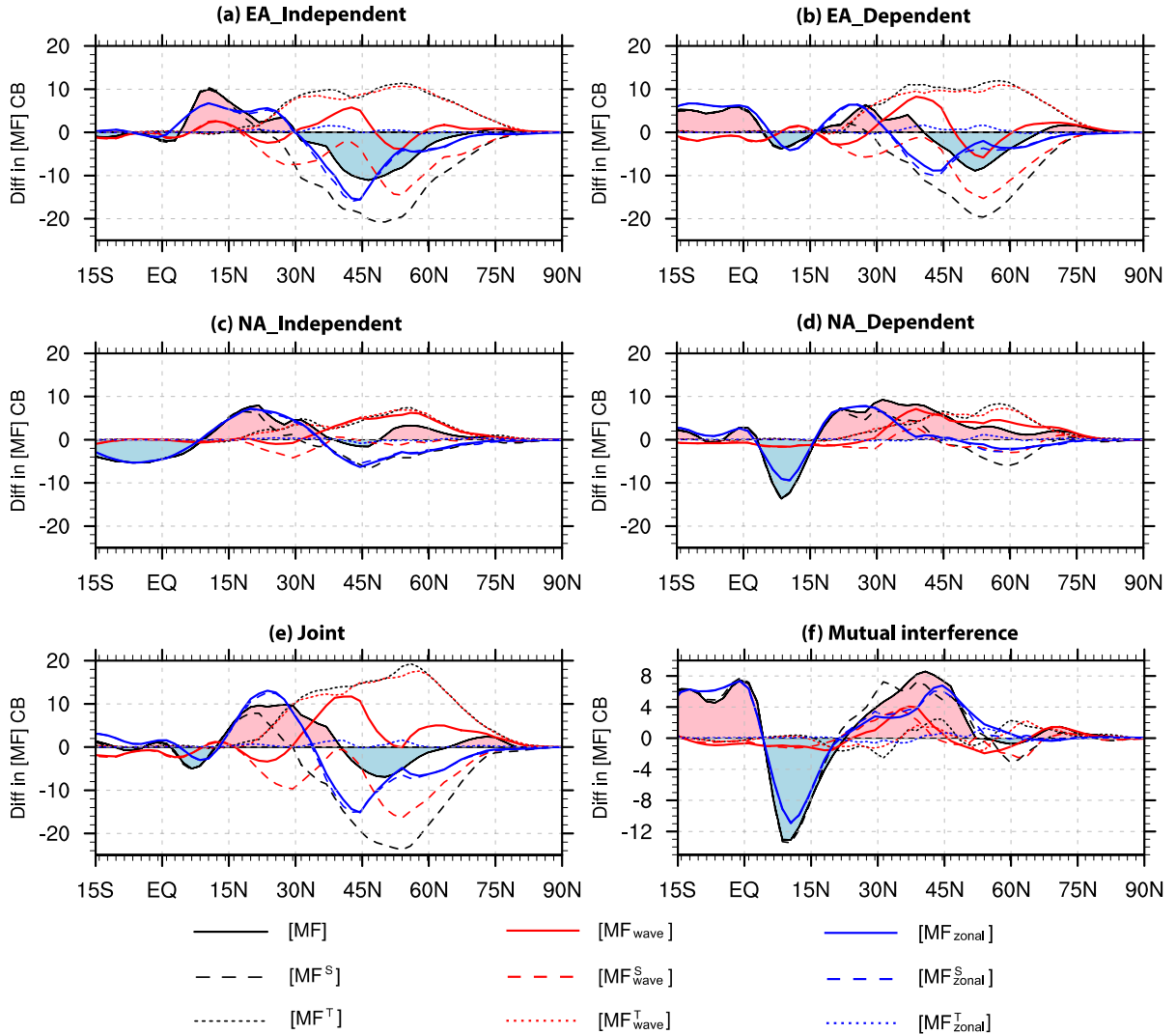
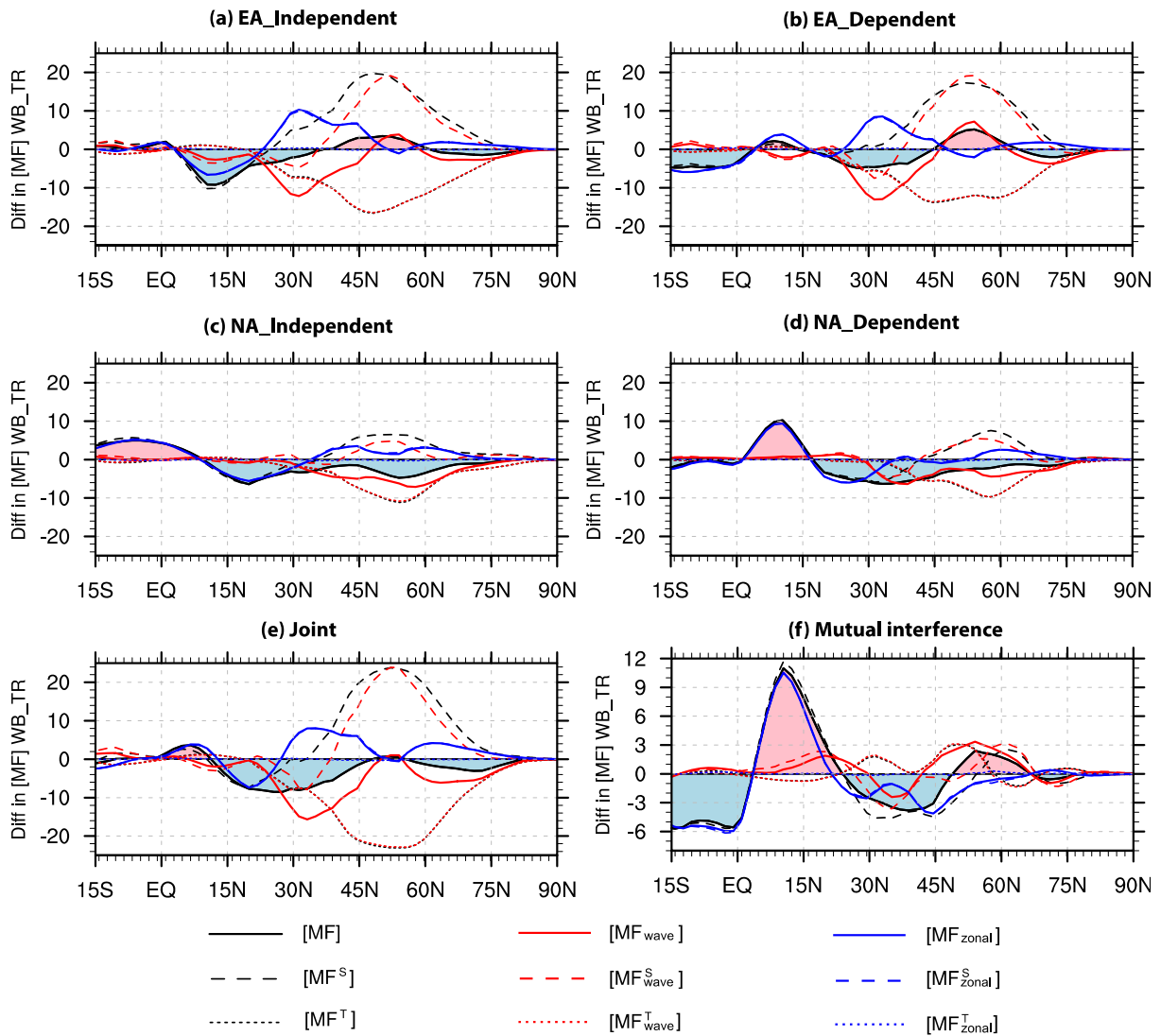


Figure 3. Topographic effects on the winter climatology of the vertical integral of [MF] within the CB of IMMC in each latitude band (black curves with red/blue shadings indicating positive/negative values, units: 10^9 kg s^{-1}) and its components driven by stationary and transient zonal-mean flow and waves.

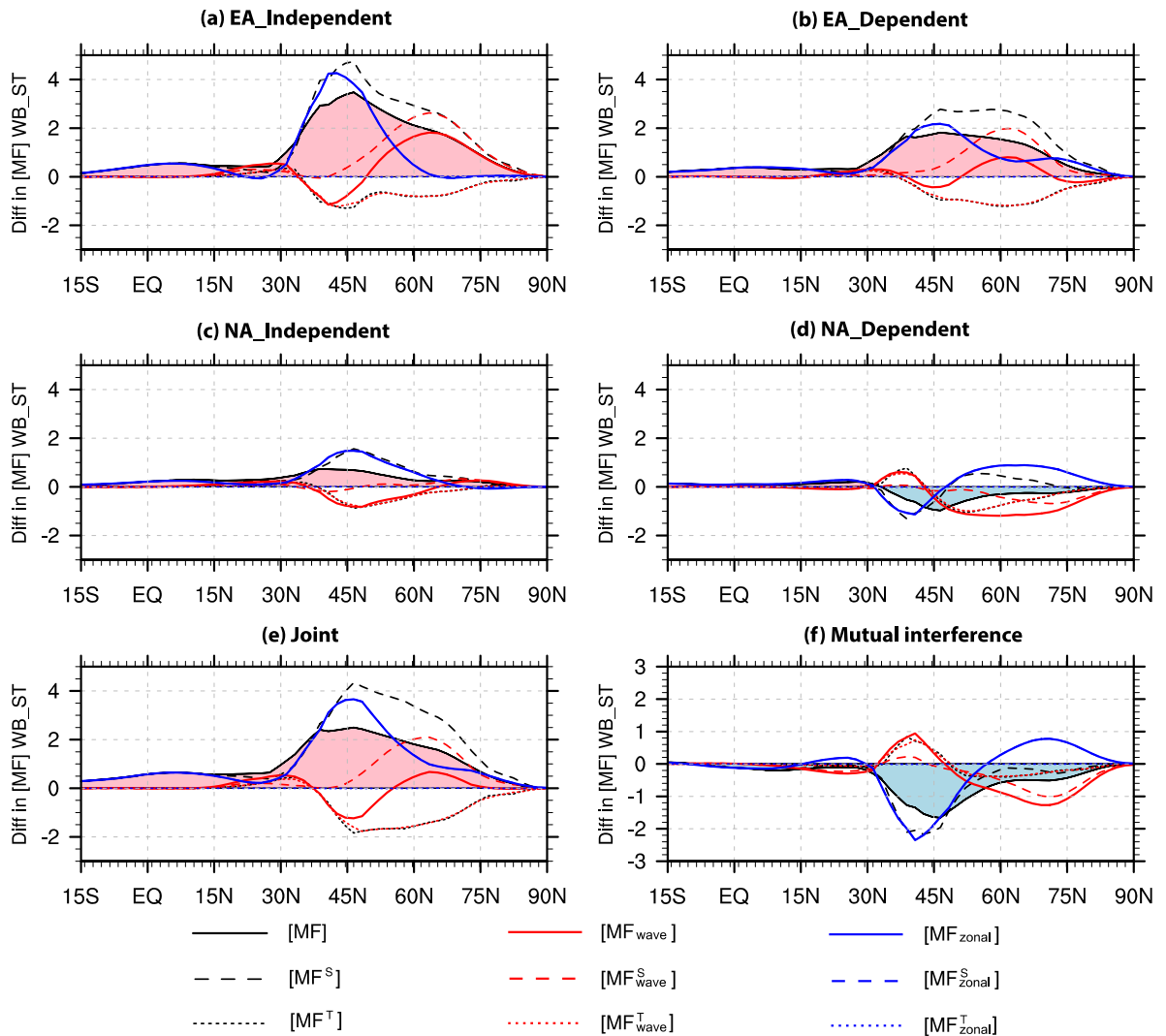
929



934

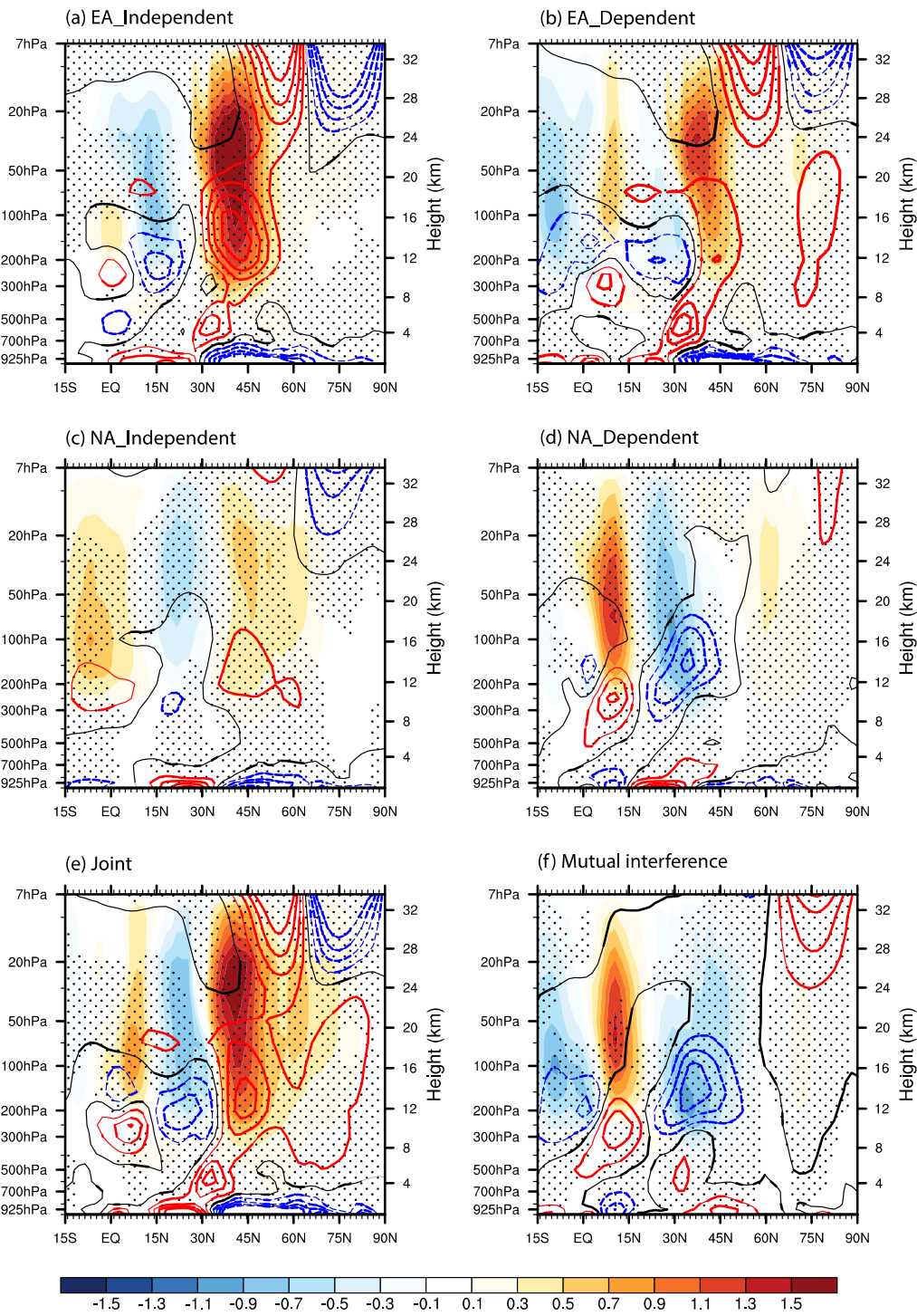
935

Figure 4. As in Fig. 3, but for the WB_TR.



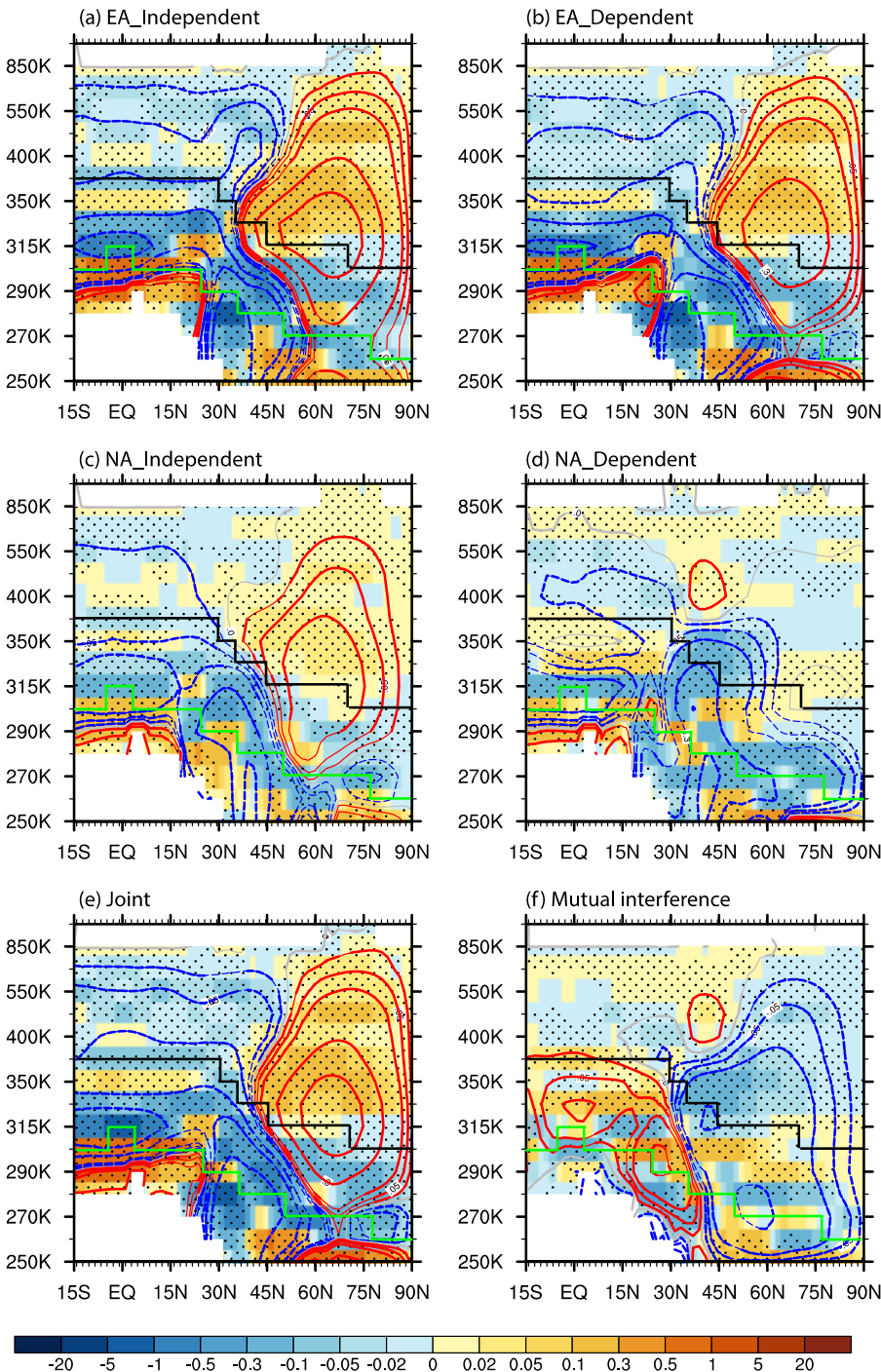
936

937 **Figure 5.** As in Fig. 3, but for the WB_ST.



938

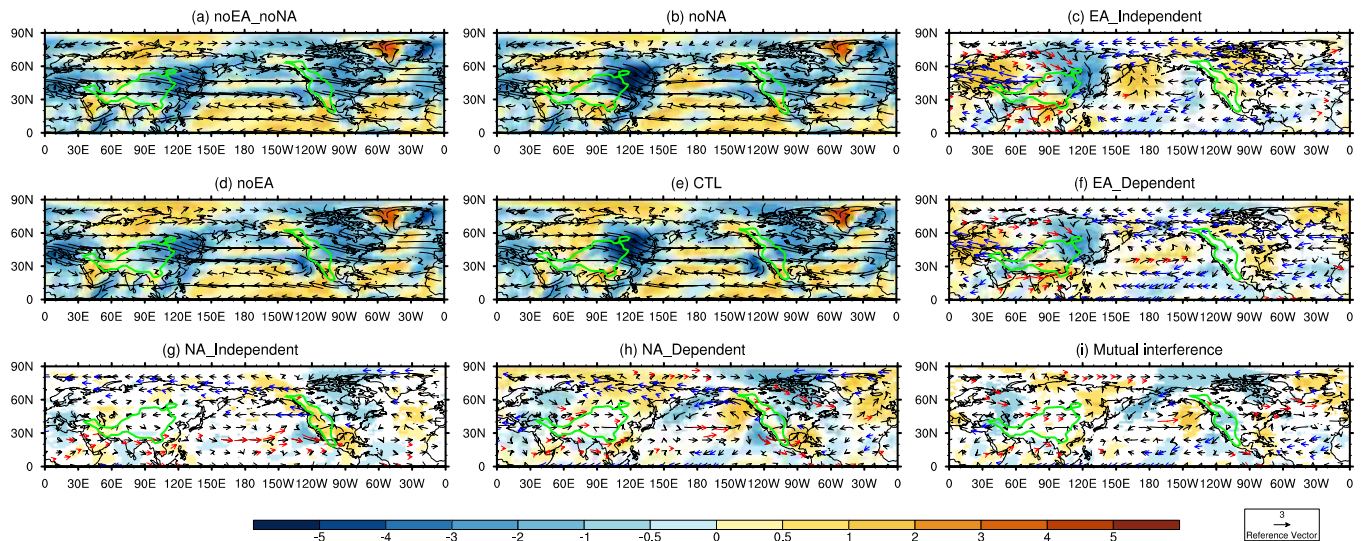
939 **Figure 6.** Topographic effects on the winter climatology of the zonal-mean meridional wind
 940 (units: m s^{-1} , contours) and mass stream function from the top (units: $10^{10} \text{ kg m s}^{-1}$, shadings)
 941 at pressure levels in the NH. Dotted areas and thickened contours mark the 95% confidence
 942 level.



943

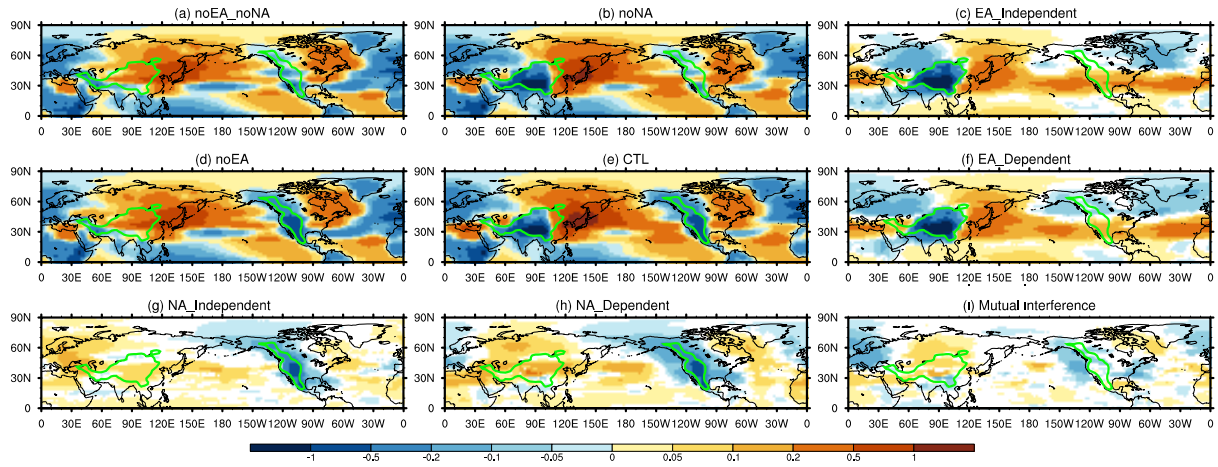
944 **Figure 7.** As in Fig. 2, but for the differences in the zonally integrated fields of isentropic
 945 layer mass (shading) and vertical integral of mass above each isentropic level (contours) in
 946 each latitudinal band in the NH (units: 10^{14} kg). Dotted areas and thickened contours mark the
 947 95% confidence level of the differences.

948



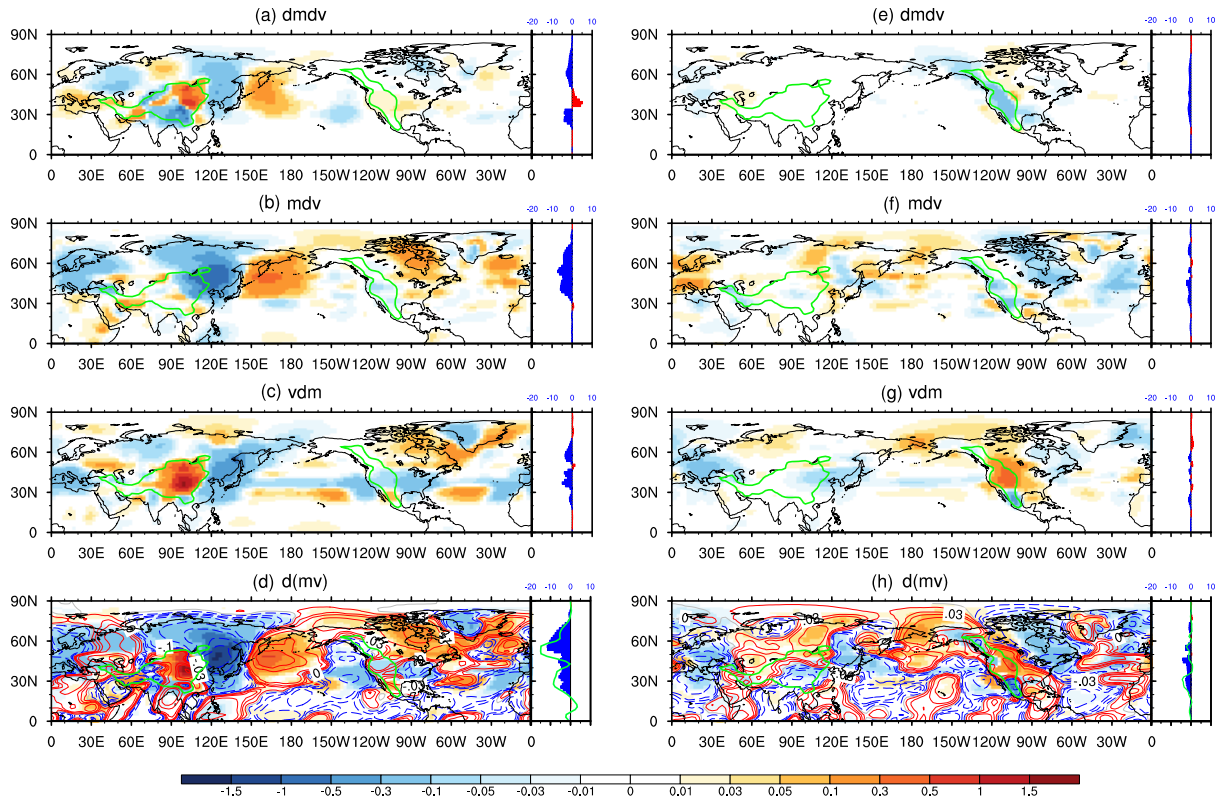
949

Figure 8. The winter climatology (a–b, d–e) and its differences among the four experiments (c, f, g–i), of the mass-weighted means of zonal wind vs. the wave component of the meridional wind within the CB (U_{CB}^S and $V_{CB_{wave}}^S$, vectors, units: $m s^{-1}$). Differences in the meridional wind velocity passing the 95% significance level are highlighted with shadings; those in the zonal wind velocity passing the 95% significance level are highlighted with colored vectors, with red/blue vectors for positive/negative values. Green contours are the regions with surface height exceeding 1000m, indicating the location of EA/NA_Topo.



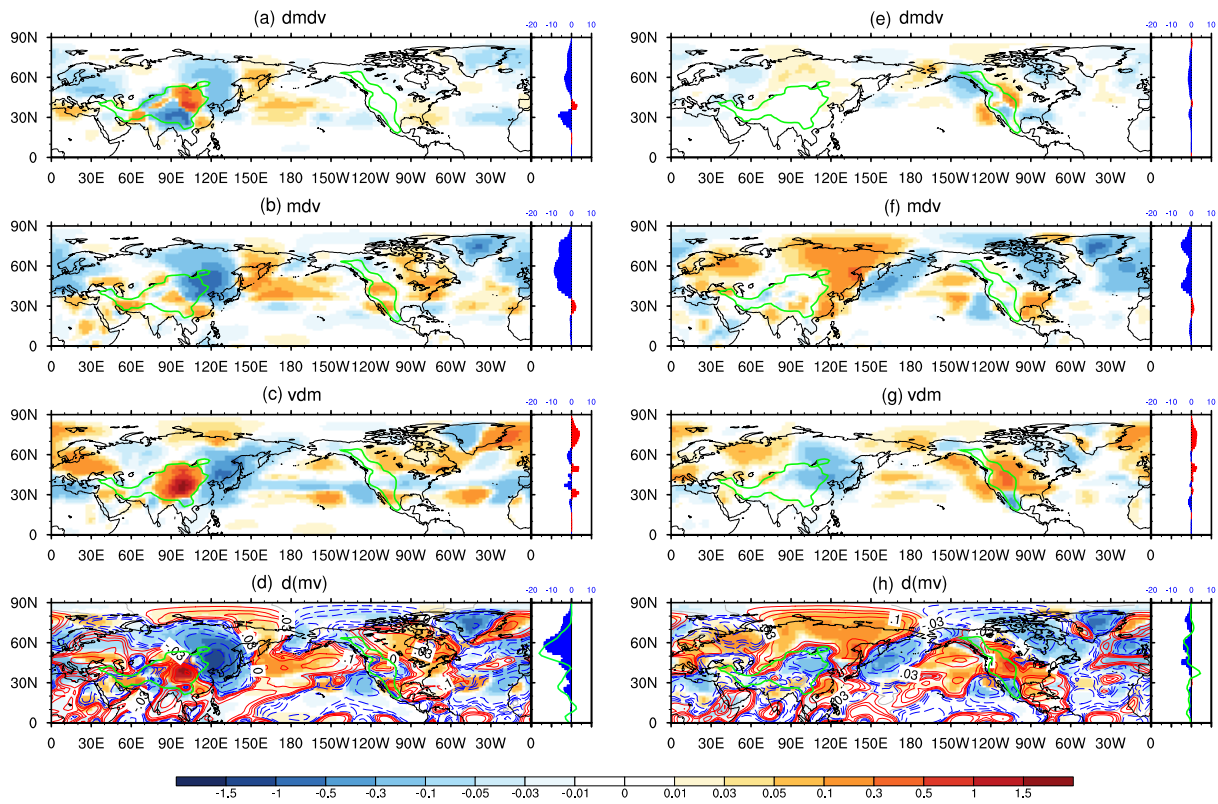
958

959 **Figure 9.** As in Fig. 8 but for the wave component of the vertical integrated air mass
 960 within the CB (units: 10^{14} kg). Only the differences above the 95% significance level are
 961 shown.



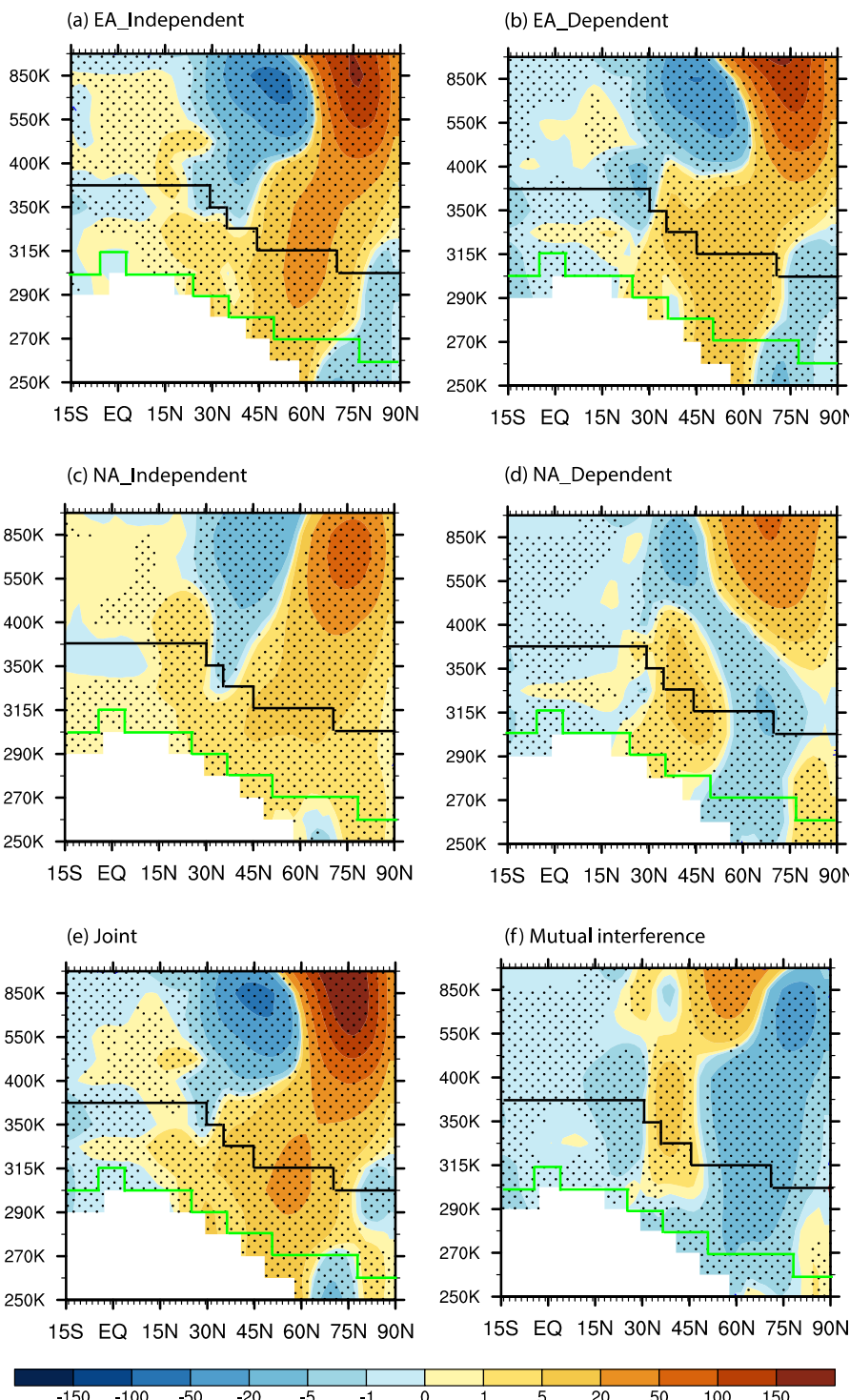
962

963 **Figure 10.** The total and linearized stationary-wave component of MF changes within the CB
 964 layer (units: 10^9 kg s^{-1}) forced by the independent EA and NA. (a) $\Delta M_{\text{CB}}^S \cdot \Delta V_{\text{CB}}^S$:
 965 the independent-EA-forced wave pattern of meridional stationary wind multiplied by the
 966 independent-EA-forced cold air mass (left panel) and its zonal integral (right panel). (b)
 967 $M_{\text{CB}}^S \cdot \Delta V_{\text{CB}}^S$: the independent-EA-forced wave pattern of meridional stationary
 968 wind multiplied by the preexisting wave pattern of cold air mass associated with the land-sea
 969 contrast (left panel) and its zonal integral (right panel). (c) $\Delta M_{\text{CB}}^S \cdot V_{\text{CB}}^S$: the
 970 independent-EA-forced wave pattern of cold air mass multiplied by the preexisting wave
 971 pattern of meridional stationary wind associated with the land-sea contrast (left panel) and its
 972 zonal integral (right panel). (d) The sum of the three terms in panels (a)–(c) (shadings in the
 973 left panel) and its zonal integral (bars in the right panel), overlaid by the vertical integral of
 974 MF_{wave}^S within the CB layer (contours in the left panel) and its zonal integral (green curves in
 975 the right panel). (e)–(h) are the same as (a)–(d), but for the independent effect of NA. Green
 976 contours indicate the location of EA/NA_Topo.



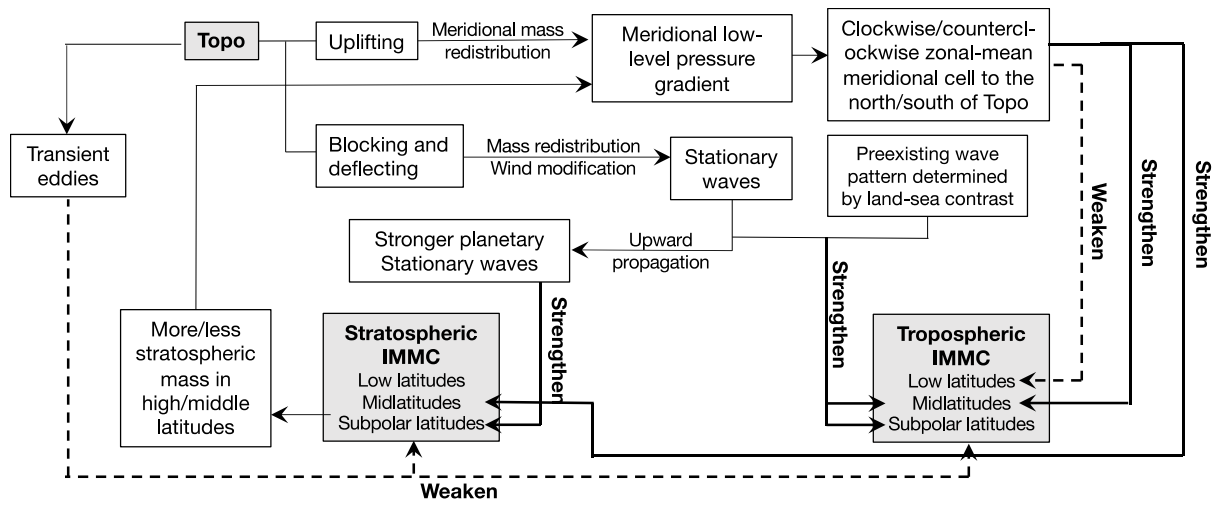
977

978 **Figure 11.** As in Fig. 10, but for the dependent effects of EA and NA when the other
979 topography exists. Note that the preexisting wave pattern of stationary meridional wind and
980 air mass in each linearized term are associated with both the land-sea contrast the NA/EA
981 topography.



982

983 **Figure 12.** As in Fig. 2, but for the differences in stationary wave amplitudes (units: m).



984

985 **Figure 13.** Schematic diagram for the key processes involved in the independent effect of EA
 986 or NA Topography on the IMMC.

Supplementary Files

This is a list of supplementary files associated with this preprint. Click to download.

- [SupplementaryMaterial.docx](#)